

20 Abstract

21 Suspended sediments (SS) contribute to the maintenance of several ecosystems. However,
22 intense soil erosion can lead to environmental, social, and economic impacts. South America
23 (SA) has very high erosion and sediment transport rates. Here we present a detailed description
24 of the spatio-temporal dynamics of natural SS flows in SA using the continental sediment model
25 MGB-SED AS. We evaluate the model with daily in-situ data from 570 stations, information
26 from regional studies and a global model. The model performance analysis showed that, in
27 general, there was a better adjustment of the simulated data with those observed than with the
28 information found in regional studies and of the global model. The use of the hydrodynamic
29 propagation method has allowed a better representation of sediment flows in rivers and
30 floodplains. Based in the calibrated model results, SA delivers 1.00×10^9 t/year of SS to the
31 oceans, in which the Amazon (3.89×10^8 t/year), Magdalena (7.57×10^7 t/year) and La Plata
32 (5.07×10^7 t/year) rivers are the main suppliers. The floodplains play an essential role, retaining
33 about 9.4% (1.11×10^8 t/year) of the SS loads reaching the rivers. In this study, datasets related to
34 SS flows in SA were generated and can be used to support other large-scale researches or
35 policymakers and stakeholders for adequate management of continental land use.

36

37 **Key words:** Continental-scale; Erosion; MUSLE; MGB

38

39 1 Introduction

40 Understanding erosion and sediment transport processes are relevant to comprehend geological
41 changes and landscape evolution (Latrubesse et al., 2005; Syvitski and Milliman, 2007; Zhang et
42 al., 2004), biogeochemical cycles (e.g., Beusen et al., 2005; Doetterl et al., 2012; Galy et al.,
43 2015; Ito, 2007; Kuhn et al., 2009; Lal, 2003; Müller-Nedebeck and Chaplot, 2015; Naipal et al.,
44 2018; Tan et al., 2017; Van Oost et al., 2007; Willenbring and Von Blanckenburg, 2010), and
45 impacts of human activities, such as land use/ land cover changes (e.g., Murphy, 2019; Oliveira
46 et al., 2015; Panagos et al., 2017; Wang and Van Oost, 2019) and dams construction (e.g., Best,
47 2019; Cohen et al., 2014; Forsberg et al., 2017; García-Ruiz et al., 2015; Latrubesse et al., 2017,
48 2005; Restrepo et al., 2006; Syvitski et al., 2005). In the last 8,000 years, the conversion of
49 natural vegetation into agriculture has resulted in an accumulated erosion of about $27,187 \pm 9,030$
50 Gt worldwide (Wang and Van Oost, 2019). Meanwhile, it is estimated that the impact of soil
51 erosion on global GDP (Gross Domestic Product) is an annual loss of ~US\$ 8 billion,
52 threatening the food security, leading to a global reduction in the production of 33.7 Gt/year and
53 a consequent increase in water withdrawals of 48 billion m³/year (Sartori et al., 2019).

54 A large number of rivers with the largest sediment transports world (>100 Mt/year) are in South
55 America (SA, Borrelli et al., 2017; Doetterl et al., 2012; Latrubesse et al., 2005; Mouyen et al.,
56 2018; Naipal et al., 2018; Syvitski et al., 2014, 2005; Wuepper et al., 2019). The Amazon River
57 is at the top of the list transporting about 1,000 Mt/year, according to Latrubesse et al. (2005).
58 Borrelli et al. (2017) observed high erosion rates (>10 t/ha.year) in SA in 2012, which increasing
59 tendency compared to the 2001 year. This severe erosion has contributed to generate, for
60 example, a reduction in food production of 8,170 Mt/year in Brazil (Sartori et al., 2019).
61 Researches have shown that climate changes will impact the land use/ land cover (Almagro et
62 al., 2017; Brêda et al., 2020; Cohen et al., 2014) and that the implementation of many dams will

63 affect even more the connectivity of water flows, sediments, nutrients, and aquatic organisms
64 (Forsberg et al., 2017; Grill et al., 2019; Latrubesse et al., 2017).

65 In the last decades, great efforts have been dedicated to understanding and quantifying sediment
66 loads around the world. The use of in-situ measured data is one of the main used tools to
67 estimate the transport in rivers (e.g., Best, 2019; Dearing and Jones, 2003; Latrubesse et al.,
68 2005; Mouyen et al., 2018; Murphy, 2019; Niu et al., 2014; Restrepo et al., 2006) or watershed
69 erosion rates (e.g., García-Ruiz et al., 2015). However, there is a lack of measurements of
70 sediments in both intra-basin (e.g., García-Ruiz et al., 2015; Kettner et al., 2010; Lima et al.,
71 2005) and near the Oceans, where less than 10% of rivers have monitoring of sediment delivery
72 to coastal zones (Syvitski et al. 2005). Notably, in the era of big data and big science, there are
73 still so few hydrological, sediment, and nutrient data available in the world's large rivers (Best,
74 2019). The lack of data represents a major barrier to develop analyses for large scales
75 (continental or global) that require long time series (Dearing and Jones, 2003).

76 Computational sediment models have helped to fill this gap of sediment information. For the
77 global scale, several applications have been carried out with Universal Soil Loss Equation
78 (USLE, e.g., Xiong et al., 2019, 2018) – developed by Wischmeier and Smith (1978) – and its
79 revised version RUSLE (e.g., Borrelli et al., 2017; Naipal et al., 2018, 2015; Sartori et al., 2019;
80 Wuepper et al., 2019; Yang et al., 2003). According to Alewell et al. (2019), USLE and RUSLE
81 are the most used models around the world. However, approaches that used these models were
82 focused only on soil loss spatial representation, with long-term average estimates, which do not
83 allow to understand the dynamic processes that involve sediment flows, such as the loads
84 transported by the rivers. In this perspective, global sediment transport models were developed to
85 estimate the impact of human activities on sediment delivery to the oceans (Syvitski et al. 2005),
86 characterize rivers in terms of transported sediment loads (Cohen et al., 2013; Pelletier, 2012),
87 and assess regional trends and variabilities (Cohen et al. 2014). The global models are generally
88 empirically-based and have few input parameters, which facilitate applications on these scales.
89 Nevertheless, these models have been poorly validated, they were focused on estimating long-
90 term annual averages (e.g., Cohen et al. 2013; Pelletier 2012; Syvitski and Milliman 2007), and
91 are based on simplified methodologies to estimate hydrological variables and sediment routing.

92 Despite the barriers encountered in the model applications on a global scale, few papers are
93 found in the literature regarding continental scales. Panagos et al. (2015) used the RUSLE2015
94 model to estimate erosion rates for the reference year 2010 across Europe, with a spatial
95 resolution of 100 m. Campagnoli (2006) used an approach (not fully described) focused on
96 geological and geomorphological aspects to generate an annual sediment yield map of South
97 America. However, as mentioned in the previous paragraph, these approaches are not capable to
98 fully describe dynamic sediment processes.

99 The global model WBMsed used by Cohen et al. (2014) uses the simplified Muskingum-Cunge
100 routing method (Wisser et al., 2010). The global models of Pelletier (2012) and Syvitski and
101 Milliman (2007) do not explicitly consider the rivers flow routing. Studies performed in several
102 South America regions have shown that simplified methods are sometimes not suitable to
103 represent backwater and floodplain effects, which can be driving factors in flow routing in large
104 basins (e.g., Angarita et al., 2018; Bravo et al., 2012; Paiva et al., 2013, 2011; Pontes et al., 2017;
105 Siqueira et al., 2018; Zhao et al., 2017).

106 On the other hand, when we compare the sediment modeling studies with hydrological-
107 hydrodynamic modeling studies, one can see that significant advances have been made in the
108 later for global and continental scales. For example, studies made by Hanasaki et al. (2006),
109 Hanasaki et al., (2008a, 2008b) and Hanasaki et al. (2018) showed global scale simulations with
110 many capabilities to represent the global hydrological cycle and the human interference on it,
111 such as water abstractions and rivers impoundments. The van Beek et al. (2011) study used the
112 global PCR-GLOBWB model to evaluate water availability and water stress on a monthly scale
113 for the whole globe. Meanwhile, the study by Beck et al. (2017) shows how extensive global
114 hydrological models development research is, while evaluating the runoff estimates generated
115 across the globe by six global models in addition to four land surface models. Other examples,
116 with a greater focus on the fluvial hydrodynamic representation, are the studies of Yamazaki et
117 al. (2011) and Yamazaki et al. (2013), which showed global model applications for flooding
118 applications, including the impact of floodplains. Also, most of the models developed in recent
119 years simulate processes on a daily scale (Bierkens, 2015). Many of them have the concept of
120 "hyperresolution models" as their motivation, which aims to simulate processes on a global
121 scale, but whose results are useful on a local scale (e.g., Bates et al., 2018; Wada et al., 2014;
122 Wood et al., 2011).

123 On the continental scale, progress in the development of hydrological and hydrodynamic models
124 also stand out, with dam representation (Shin et al., 2019) and improvements in fluvial
125 hydrodynamics (Siqueira et al., 2018). The National Water Model (NWM,
126 <http://water.noaa.gov/about/nwm>) developed in 2016 by National Oceanic and Atmospheric
127 Administration (NOAA), which has been conducting simulations and streamflow forecasts for
128 the United States, can be mentioned as an example. Especially the study of Siqueira et al. (2018)
129 applied for the first time a continental-scale fully coupled hydrological-hydrodynamic model for
130 the whole South America. The Siqueira et al. (2018) results showed that limitations on flow
131 estimation by state-of-the-art global models could be reduced using better calibrated continental
132 models, which represent relevant processes (e.g., hydrodynamics) for the area of interest, and
133 which are built on previous experience of regional-scale studies.

134 While these cited examples of hydrologic and hydrodynamic modeling with continental and
135 global scales have increasingly appeared in the literature, including the goal of attaining
136 "hyperresolution" models, no study has been found in the literature to estimate continental-scale
137 sediment transport having hydrologic-hydrodynamic processes integrated. There is then a gap
138 between the advances in large scale hydrologic and hydrodynamic modeling and the advances in
139 sediment modeling at continental and global scales.

140 Bridging the gaps between recent advances in hydrologic and hydrodynamic modeling at
141 continental scales and sediment modeling provide some opportunities: (i) obtain models that
142 allow the comprehension and comparison of spatial and temporal dynamics explicitly, and that
143 still represent important processes such as backwater effects in the rivers and the lateral flow
144 exchange of water and sediments with floodplains (e.g., Buarque, 2015; Cohen et al., 2013; Grill
145 et al., 2019; Paiva et al., 2013, 2011; Pontes et al., 2017; Rudorff et al., 2018); (ii) obtain
146 continental or global scale models that are well-validated to provide locally relevant information
147 at multiple time scales and suitable for policymakers and stakeholders (Bierkens, 2015;
148 Fleischmann et al., 2019b; Siqueira et al., 2018); (iii) acquire continental sediment discharges
149 information not only in the outlets of large rivers but also intra-basin. These items, therefore,
150 become the interest of this study, which has South America as a subject of study, and aims to

151 answer the following specific questions from modeling results: what is the accuracy of the
152 proposed continental sediment model? What is the potential transported loads by the rivers in the
153 continent? What are the spatial and temporal dynamics of sediment flows over South America?
154 What is the impact of fluvial hydrodynamics on sediment transport and deposition? In which
155 regions do suspended sediments deposit the most? To answer these questions, we have
156 developed and evaluated the performance of sediment erosion and transport model for the entire
157 South American domain.

158 **2 Overview of Sediment-Related Processes in South America**

159 South America (SA) transports ~20% of the sediments reaching the oceans (Syvitski et al.,
160 2005), and the Amazon and Magdalena rivers (Figure 1: South America showing: a) major hydrological
161 regions according to FAO and Agência Nacional de Águas do Brasil (ANA) classifications, relief map based on the
162 Bare-Earth SRTM (O'Loughlin et al., 2016), including main rivers, flooded areas (Fluet-Chouinard et al., 2015) and
163 artificial lakes (Lehner et al., 2011); and b) existent dams from GRanD v1.3 product ($>0.1 \text{ km}^3$ Lehner et al., 2011 -
164 <http://globaldamwatch.org>) and from ANA ($> 30\text{MW}$), and sediment stations from ANA, Base de Datos
165 Hidrológica Integrada da Argentina (BDHI) and Instituto de Hidrologia, Meteorologia e Estudos Ambientais da
166 Colômbia (IDEAM). -a) are among the world's largest sediment delivers (Mouyen et al., 2018). SA
167 has the second-highest potential erosion rate on the planet and the highest increase in the last
168 century (Wuepper et al., 2019). This increase also attributes to SA the highest rate of particulate
169 organic carbon erosion. (Naipal et al., 2018). Among the causes of these changes are agricultural
170 expansion and deforestation (Borrelli et al., 2017), which have been increasing, causing concerns
171 in the Amazon basin (Aguiar et al., 2016; Aragão, 2012).

172 Most of the SA is located in tropical regions that have little variability between sunrise and
173 sunset and receive high solar incidence. The Intertropical Convergence Zone (ITCZ) directly
174 influences the establishment of dry and rainy seasons; El Niño events; and the South Atlantic
175 Convergence Zone (SACZ), which causes heavy precipitations in the summer. Annual
176 precipitation variability is strong, with desert regions in Chile and rainfall reaching
177 approximately 10,000 mm in Colombia (Latrubesse et al., 2005).

178 Rivers that drain the Andean region transport the highest sediment load on the continent.
179 According to Restrepo et al. (2006), the Magdalena River is the one with the highest average
180 sediment yield ($690 \text{ t/km}^2\cdot\text{year}$). More than 90% of the suspended sediment (SS) load of the
181 Amazon Basin comes from the Andes (Latrubesse et al., 2005). Filizola and Guyot (2011), using
182 in-situ measured data, indicate that the Madeira River (Figure 1: South America showing: a) major
183 hydrological regions according to FAO and Agência Nacional de Águas do Brasil (ANA) classifications, relief map
184 based on the Bare-Earth SRTM (O'Loughlin et al., 2016), including main rivers, flooded areas (Fluet-Chouinard et
185 al., 2015) and artificial lakes (Lehner et al., 2011); and b) existent dams from GRanD v1.3 product ($>0.1 \text{ km}^3$ Lehner
186 et al., 2011 - <http://globaldamwatch.org>) and from ANA ($> 30\text{MW}$), and sediment stations from ANA, Base de
187 Datos Hidrológica Integrada da Argentina (BDHI) and Instituto de Hidrologia, Meteorologia e Estudos Ambientais
188 da Colômbia (IDEAM). -a) contributes almost 50% to the Amazon River solid discharge, in which
189 the Beni and Mamoré rivers represent about 72% and 28%, respectively, of the Madeira
190 transport. (Guyot et al., 1999). The Ucayali River drains the Peruvian Andean part and is also
191 one of the SA rivers with the highest SS load (Latrubesse et al., 2005). Rivers originating in the
192 South Andean regions also carry high SS loads, such as the Bermejo River, which provides about
193 90% (Amsler and Drago, 2009) and the Pilcomayo river about 140 Mt/year of the total load
194 carried by the Paraná River (Latrubesse et al., 2005). Lima et al. (2005) observed that smaller
195 rivers like Parnaíba, Paraíba do Sul and Doce (Figure 1-a), although they do not have the highest
196 sediment yield rates (t/year.km^2), they have high values of suspended sediment concentrations

220 FAO and Agência Nacional de Águas do Brasil (ANA) classifications, relief map based on the Bare-Earth SRTM
221 (O'Loughlin et al., 2016), including main rivers, flooded areas (Fluet-Chouinard et al., 2015) and artificial lakes
222 (Lehner et al., 2011); and b) existent dams from GRanD v1.3 product ($>0.1 \text{ km}^3$ Lehner et al., 2011 -
223 <http://globaldamwatch.org>) and from ANA ($> 30\text{MW}$), and sediment stations from ANA, Base de Datos
224 Hidrológica Integrada da Argentina (BDHI) and Instituto de Hidrologia, Meteorologia e Estudos Ambientais da
225 Colômbia (IDEAM). -a), which cause disturbances in river systems, decreasing the sediment load
226 and affecting the geomorphology and the downstream floodplain productivity (Almeida et al.,
227 2015; Grill et al., 2019; Latrubesse et al., 2017, 2005; Restrepo et al., 2006). The highest
228 sediment trap rates in SA dams are found in the Amazonian rivers such as Madeira (e.g., Rivera
229 et al. 2019), Upper Solimões and Tapajós (e.g., Latrubesse et al. 2017), and in São Francisco,
230 Tocantins and Paraná rivers (e.g., Syvitski et al. 2005).

231 Despite the knowledge provided by previous studies, some things are not yet fully understood:
232 the effect of fluvial hydrodynamics on sediment flows; thoroughly and accurately, the
233 spatiotemporal patterns of denudation rates, concentration (SSC), solid discharge (QSS) and
234 suspended sediment deposition; the driving factors in the relation between SSC/QSS and water
235 discharge; the annual sediment balance of the SA and its main rivers; the potential consequences
236 of climate changes on the patterns of these variables; the impact of dams on rivers and those with
237 the greatest potential to be affected; the relevance of landslides in the sediments transport of each
238 river; and the relative contribution of the anthropic activities, such as mining, to the sediment
239 flows.

240 **3 South America Sediment Model**

241 To comprehend South America sediment flows, we used the MGB-SED sediment model
242 (Buarque, 2015; Fagundes et al., 2019, 2020; Föeger, 2019) coupled to hydrologic-
243 hydrodynamic model MGB AS, presented by Siqueira et al. (2018). This modeling configuration
244 was chosen for three main reasons: (i) it is the first fully coupled hydrologic-hydrodynamic
245 model, developed for regional scales, applied for South America's continental domain; (ii) the
246 model has a high temporal resolution (daily outputs) and was validated in most of SA using in-
247 situ and other sources of hydrological data, showing that hydrological variables were well
248 represented; and (iii) the performance of sediment models can be strongly affected by the
249 performance of hydrological models (Cohen et al., 2013; Shen et al., 2012), and the MGB AS
250 has a better performance compared to the global models evaluated by Siqueira et al. (2018).

251 **3.1 MGB AS Hydrologic-Hydrodynamic Model**

252 The *Modelo Hidrológico de Grandes Bacias* (MGB) was initially developed by Collischonn et
253 al. (2007) and further improved to address different questions (e.g., Fleischmann et al., 2019,
254 2018; Paiva et al., 2011; Pontes et al., 2017; Siqueira et al., 2018). It is a conceptual model, semi-
255 distributed, and has spatial discretization defined by unit catchments (Pontes et al., 2017), each
256 with its own river stretch and floodplain. Precipitation is the main driver of the model (it does not
257 consider snow or ice melting), from which hydrological processes are simulated, such as: canopy
258 interception, soil infiltration, evapotranspiration, and routing of surface, subsurface and
259 groundwater flows. Each unit catchment can have several Hydrological Response Unit (HRU),
260 which is a combination of soil type and soil cover (Kouwen et al., 1993), where water and energy
261 are computed. Surface, subsurface, and groundwater volumes are stored in simple linear
262 reservoirs and further routed to the stream network.

263 In the following, a brief description of the methodology used by Siqueira et al. (2018) is
264 presented. We use the same MGB AS settings and structure, as well as the input data used by the
265 authors. They found agreement between the simulated and observed flows that resulted in a
266 Nash-Sutcliffe efficiency coefficient (NSE) > 0.6 in more than 55% of the analysed stations.

267 Flow routing in the drainage network is performed using the local inertial method (Bates et al.,
268 2010; Pontes et al., 2017). The continuity equation is used to estimate the stored volume, flooded
269 area, and streamflow and floodplain water level. Floodplains are represented as storage areas that
270 compute evaporation in open waters, assuming that water level is constant for the whole unit
271 catchment. Floodplains water infiltration for unsaturated soils are still considered (as described
272 by Fleischmann et al. 2018), specifically for the Pantanal wetlands.

273 MGB AS model also allows using the Muskingum-Cunge (MC) method to routing flows. This
274 method takes a time interval that is subdivided into smaller intervals and also split the total river
275 reach length into sub-reaches to route the flows. The MC method enables the representation of
276 flood wave translation and smoothing, that routes at a velocity c (celerity) higher than average
277 streamflow velocity in a specific time interval and river reach. Among the method advantages
278 are the more straightforward implementation, lower computational efforts, and numeric stability.
279 As for disadvantages, there are the non-representation of backwater effects and lateral exchanges
280 between river and floodplain, which may play an important role in large basins (Getirana and
281 Paiva, 2013).

282 In the MGB AS pre-processing, Siqueira et al. (2018) used the flow direction map from
283 HydroSHEDS, 15arcsec (Lehner et al., 2008), a 1,000km² drainage area threshold to onset the
284 river network, and unit catchments and river reaches were delineated using a fixed-length vector-
285 based discretization of $\Delta x=15$ km. The Digital Elevation Model (DEM) Bare-Earth SRTM v.1
286 (O’Loughlin et al., 2016) was used to compute the Height Above Nearest Drainage (HAND),
287 from which the floodplain topography was estimated at a sub-grid level. River hydraulic
288 geometry was set using the global data set of Andreadis et al. (2013), enhanced using
289 information from regional studies (Beighley and Gummadi, 2011; Paiva et al., 2013, 2011;
290 Pontes, 2016).

291 Precipitation data from global Multi-Source Weighted Ensemble Precipitation – MSWEP v1.1
292 (Beck et al., 2017) were used. The climatic variables used to estimate evapotranspiration were
293 temperature, atmospheric pressure, income shortwave solar radiation, relative humidity, and
294 wind speed obtained from Climate Research Unit (CRU) Global Climate v.2 (New et al., 2002).
295 They are long-term monthly averages (1961-1990) and have 10’ spatial resolution. South
296 America HRUs map from Fan et al. (2015) was used to represent soil type (shallow and deep)
297 and soil cover.

298 For more details about approaches, equations, and data, a full description can be found in
299 Siqueira et al. (2018).

300 3.2 MGB-SED sediment model

301 The *Modelo de Sedimentos de Grandes Bacias* (MGB-SED) was firstly introduced by Buarque
302 (2015) and improved in other studies (e.g., Fagundes et al., 2020; Fagundes et al., 2019; Föeger,
303 2019). The MGB-SED has three modules (basin, river and floodplain) and enables the simulation
304 of rill and interrill erosion processes in hillsides, bed river erosion and deposition, sediment
305 transport through the river network, and deposition of suspended sediment in the floodplains.

306 The sediment volumes from hillsides to river reaches in each unit catchment is the primary
 307 information estimated by the model using the Modified Universal Soil Loss Equation (MUSLE)
 308 (MUSLE, Williams, 1975) :

$$Sed = \alpha \cdot (Q_{sur} * q_{peak} * A)^{\beta} \cdot K \cdot C \cdot P \cdot LS_{2D} \quad (1)$$

309 where Sed [t/day] is the sediment yield, Q_{sur} [mm/day] is the specific runoff volume, q_{peak} [m³/s]
 310 is the peak runoff rate, A [ha] is the unit catchment area, K [0.013.t.m².h./m³.t.cm] is the soil
 311 erodibility factor, C [-] is the cover and management practices factor, P [-] is the conservation
 312 practices factor, LS_{2D} [-] is a bidimensional topographic factor; and α and β are the fit
 313 coefficients of the equation (which are calibrated afterward), whose values originally estimated
 314 by Williams (1975) were 11.8 and 0.56, respectively.

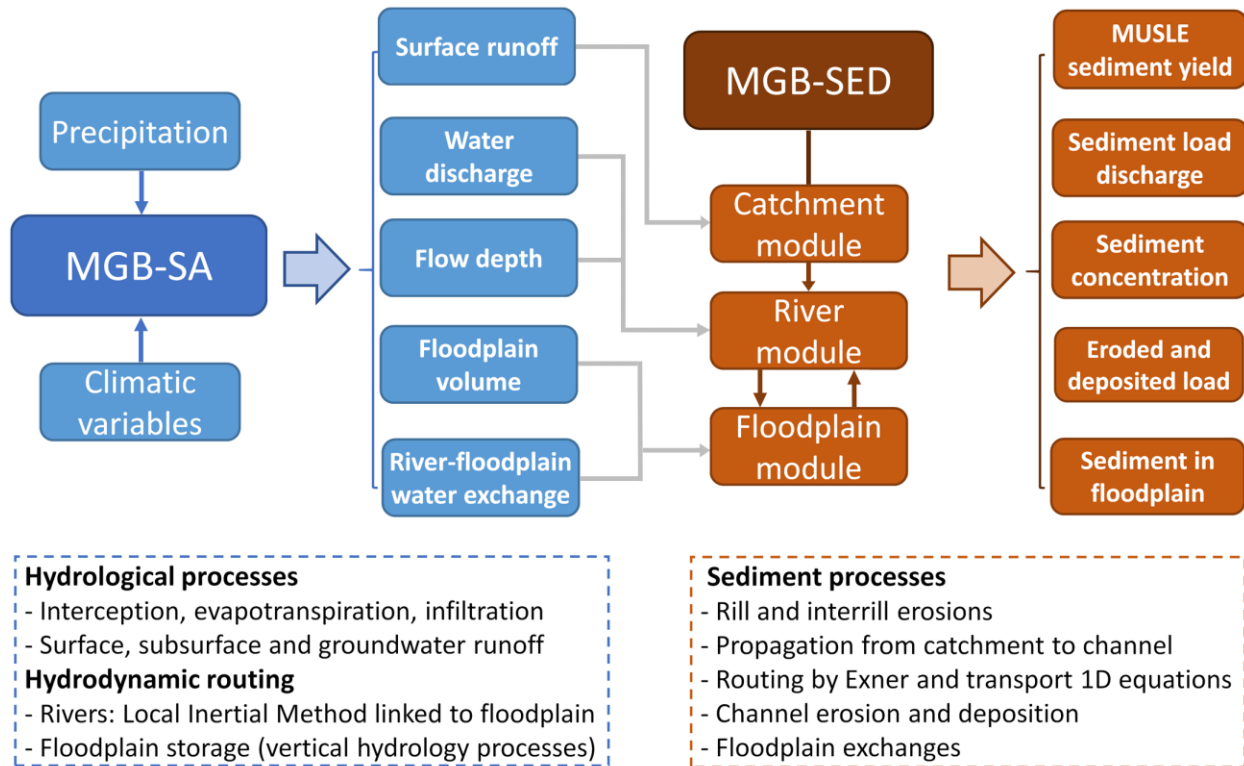
315 Q_{sur} and q_{peak} values are estimated by the coupled hydrologic model (MGB AS in this study). P
 316 factor is estimated from the knowledge of soil management and conservation practices but has
 317 been adopted as 1 in most large scale applications (e.g., Benavidez et al. 2018; Borrelli et al.
 318 2017; Naipal et al. 2015; Phinzi and Ngetar 2019). C factor is usually calculated from field
 319 experiments but has been usually adopted from literature for each soil cover, as presented by
 320 Benavidez et al. (2018) and Phinzi and Ngetar (2019). MGB-SED model computes K factor
 321 from Williams (1995) equation, in which considers the soil texture (sand, silt and clay
 322 percentages) and amount of soil organic carbon. LS_{2D} factor is estimated by the model using a
 323 DEM (Buarque, 2015) and more details about the LS_{2D} estimates can be verified in the
 324 supplementary material S1.

325 The approach used by MGB-SED to estimate sediment yield using MUSLE equation is the same
 326 used in other models, as SWAT (Arnold et al., 1998), CREAMS (Knisel, 1980), PERFECT
 327 (Littleboy et al., 1992) and SWIM (Krysanova et al., 1998). We know the limits of this approach,
 328 for example, it does not explicitly consider all erosive processes, such as those related to mass
 329 movements. Studies such as Tan et al. (2018) have already improved the estimates of a sediment
 330 model by including the representation of shallow landslides. However, as an initial approach and
 331 because it has already presented itself sufficiently in other large-scale modeling applications
 332 (e.g., Buarque, 2015), we use it, and we are aware of the limitations it imposes on the analysis of
 333 the results.

334 After computing sediment yield by MUSLE, the estimated volume is divided into three classes
 335 of particle sizes (silt, clay and sand), according to the percentage of these classes in the soil.
 336 Three linear reservoirs (one for each class) are used for the sediment routing from the hillsides to
 337 the drainage network. Each soil particle size is then routed from upstream to downstream using
 338 the following approaches: (i) for the fine loads (silt and clay), the unidimensional transport
 339 equation without the diffusion term is used, and the sediments are transported in suspension,
 340 without deposition in the channel; (ii) for sand, considered as bed load, the Exner sediment
 341 continuity equation is used together with the Yang transport capacity equation (Yang, 1973) to
 342 quantify the transport in the channel, the erosion or deposition in the bed.

343 In the floodplains, a zero longitudinal velocity is assumed, and only river-floodplain exchanges
 344 are possible. The perfect mixing in the floodplains is also assumed, which implies constant
 345 concentrations of silt and clay in the vertical profile. Floodplains working as storage areas, where
 346 fine particles can be deposited but cannot be resuspended.

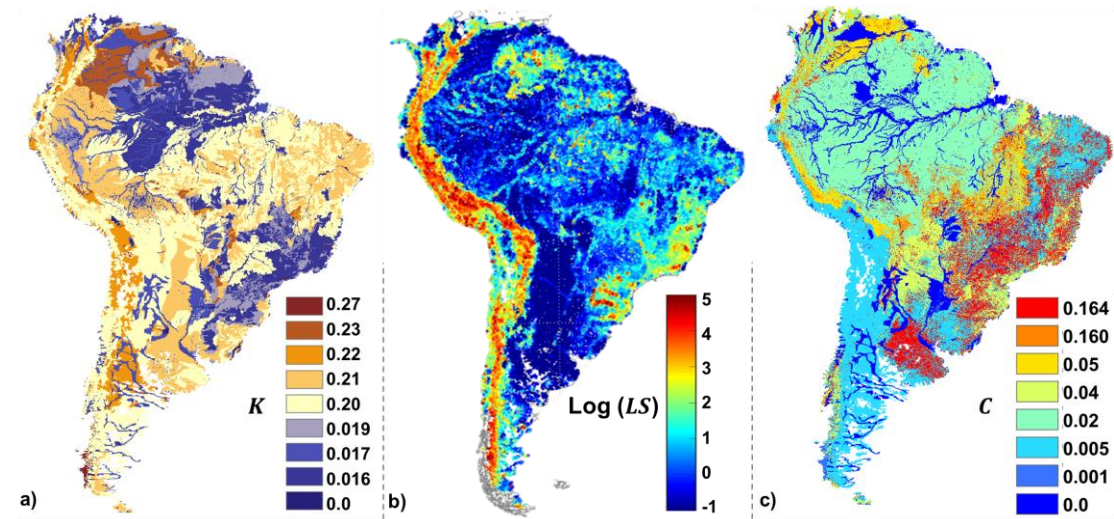
347 More details about model equations can be found in the supplementary material S1. A summary
 348 of the coupling between the two models that resulted in the MGB-SED AS, main input data,
 349 processes, and outputs are shown in Figure 2: MGB-SED AS scheme. The blue (brown) part is related to
 350 the hydrological (sediment) model, its structure, main input data, processes, and main outputs..



351
 352 **Figure 2:** MGB-SED AS scheme. The blue (brown) part is related to the hydrological (sediment) model, its
 353 structure, main input data, processes, and main outputs.

354 **3.3 Simulation Input Datasets**

355 MGB-SED model requires topographic, soil type, texture and cover, and surface runoff to
 356 estimate daily sediments using the MUSLE equation. To compute K factor (Figure 3-a), we use
 357 percentages of silt, clay, sand and organic carbon for each soil type from the Food and
 358 Agriculture Organization (FAO) of the United Nations (FAO/UNESCO, 1974). LS_{2D} factor
 359 (Figure 3-b) was estimated using Bare-Earth SRTM v.1 DEM (O’Loughlin et al., 2016). We use
 360 each land cover identified in URH South America map (Fan et al., 2015) to compute C factor
 361 (Figure 3-c) based on previous studies (Benavidez et al., 2018; Buarque, 2015; Fagundes et al.,
 362 2019). It is worth mentioning that C values for the forest were not the same throughout SA, due
 363 to the heterogeneity of forest coverings. P factor was adopted equal to 1, since in that scale there
 364 is no detailed information about soil conservation practices.



365

366 **Figure 3:** MUSLE parameters adopted for South America: a) K [0.013.t.m².h./m³.t.cm] factor; b) $\text{Log}(LS_{2D})$ [-]
367 factor; and c) C [-] factor.

368 As mentioned before, the daily runoff was estimated by MGB AS and it was also used to
369 compute q_{peak} . From this data and other simulated hydrological variables (e.g., river discharge
370 and water level, and floodplains stored volumes), it was possible to compute soil loss and
371 sediment transport using the same spatial discretization of MGB AS. We have chosen to change
372 the values of the adjustable parameters α and β , as it has been done in several works (see the
373 review presented by Sadeghi et al. (2014)), including previous applications with the MGB-SED
374 model (e.g., Fagundes et al., 2019).

375 3.4 Experimental Design

376 3.4.1 Model Calibration and Evaluation

377 The base period for the analysis and performed simulations using the MGB-SED AS model was
378 1990-2009, in which the first two years were used to warm up the model. Initially, we performed
379 a mass balance to check if the model was generating numerical errors, adding or removing mass
380 in the simulation.

381 In order to know the natural (without impoundments) simulated sediment loads transported by
382 the rivers, it was necessary to evaluate the performance of the MGB-SED AS model. For that,
383 we used suspended sediment discharge (QSS) of the 570 in-situ stations (Figure 1: South America
384 showing: a) major hydrological regions according to FAO and Agência Nacional de Águas do Brasil (ANA)
385 classifications, relief map based on the Bare-Earth SRTM (O'Loughlin et al., 2016), including main rivers, flooded
386 areas (Fluet-Chouinard et al., 2015) and artificial lakes (Lehner et al., 2011); and b) existent dams from GRanD v1.3
387 product (>0.1 km³ Lehner et al., 2011 - <http://globaldamwatch.org>) and from ANA (> 30 MW), and sediment
388 stations from ANA, Base de Datos Hidrológica Integrada da Argentina (BDHI) and Instituto de Hidrologia,
389 Meteorologia e Estudos Ambientais da Colômbia (IDEAM). -b) in Brazil - ANA (450), Colombia -
390 IDEAM (109) and Argentina – BDHI. To better explore the data, stations having at least 4
391 measurements in the period of 1992-2009 and drainage area above 1,000 km² were selected.

392 In the calibration (2002-2009), 64 stations were used, with drainage areas ranging from 3,045 to
393 4,700,503 km². The calibration stations were selected as follows: i) we always choose stations
394 with the largest drainage area for each monitored sub-basin; ii) in case stations were located

395 downstream of one (or more) reservoir (Figure 1), the one upstream with the largest drainage
 396 area would be used; iii) when there was just one station in a sub-basin, it was used to calibrate
 397 the model. The exception was Brazo Largo. If we applied these rules to this station, most of the
 398 basin of the La Plata river would not be calibrated, mainly due to lack of data in the western part
 399 of the basin and so many dams in the Paraná river (Figure 1)

400 The calibration was performed in two stages: an automatic calibration followed by a manual
 401 calibration. Automatic calibration was performed with the optimization algorithm MOCOM-UA
 402 (Yapo et al., 1998) and based on the recommendations proposed by Fagundes et al., (2019). A
 403 population of 100 individuals was used; three objective functions: Nash-Sutcliffe (*NSE*, Nash-
 404 Sutcliffe, 1970) efficiency coefficient, *BIAS*, and duration curve slope error between 10% and
 405 50% (*DCPerm*, Kollat et al., 2012); maximum of 500 iterations; and α , β and Υ (Equation 2)
 406 calibrated parameters was adjusted to each sub-basin.

$$t = \Upsilon \cdot TKS \quad (2)$$

407 *TKS* (s) is the parameter which indicates the delay time of the surface linear reservoir output; t
 408 (s) indicates the travel time of the sediments to the drainage network (see supplementary material
 409 S1); Υ [-] is the adjustment factor between the two aforementioned parameters. The range of the
 410 calibrated parameters α, β and Υ was, respectively, 0.01-25.0, 0.1-0.5 and 0.1-5.0.

411 For the basins where we did not get data, a simple transfer of parameters from the calibrated sub-
 412 basins was made. The transfer process was based on the physical and climatic characteristics of
 413 the region.

414 For the validation (1992-2009), the same criteria of the calibration stage were used, resulting in
 415 the selection of 52 sediment stations. A global evaluation of the model performance was carried
 416 out using the 570 stations. It was a conservative decision, which includes the model evaluation
 417 for the 1992-2009 period with the stations used (64) and those not used (506) in the calibration
 418 process. In addition to the metrics already mentioned, the model performance was evaluated
 419 using Pearson's correlation coefficient (*r*), Kling-Gupta (*KGE*) efficiency coefficient and
 420 relative value of Root Mean Square Error (*RMSE*).

421 MGB-SED AS results were compared to estimates from the regional studies of Latrubesse et al.
 422 2005, Lima et al. 2005 e Restrepo et al. 2006. The comparison was performed using data of long-
 423 term average annual QSS from 47 sites exceeding a drainage area of 5,000 km² (see Table1 and
 424 Figure 1, supplementary material S2). The agreement between QSS simulated and those of
 425 regional studies was evaluated from the relative difference between the annual values (Equation
 426 3).

$$Diff(\%) = 100x \frac{QSS \text{ MGB-SED AS} - QSS \text{ reg. studies}}{QSS \text{ reg. studies}} \quad (3)$$

427 Positive (negative) *Diff* values mean that MGB-SED AS model calculated values higher
 428 (lower) than those from regional studies used in the comparison.

429 QSS simulated was also compared to the outputs of the global sediment model WBMsed (Cohen
 430 et al., 2014). This model was selected because it is the only one with data freely available for
 431 society. It is a grid model with 6 arc-min (~11km) spatial resolution and uses the Muskingum-
 432 Cunge method to route daily water streamflows (Wisser et al., 2010). To estimate the QSS,
 433 firstly, the model computes the long-term average values using global empirical equation

434 BQART (Syvitski and Milliman, 2007) and then it uses the Psi model (Morehead et al., 2003) to
435 compute daily data. In the version presented by Cohen et al. (2014) the floodplains were
436 represented as temporary (final) storage areas for water (sediment). It means that the flows reach
437 the floodplains when the bankfull discharge is exceeded, and water can return to the river when
438 discharge is below bankfull.

439 The *Diff*(%) was also used for the comparisons between MGB-SED AS and WBMsed outputs
440 in 21 sites (see Table 2 and Figure 1, supplementary material S2). The WBMsed grid cells
441 identification was performed manually, and the selected sites are the same as the in-situ stations
442 used for the comparisons against regional studies, which enable contrasts between scales and
443 studies. Long-term average QSS were computed with both models in the period 1993-2009. The
444 WBMsed outputs can be obtained at <https://sdml.ua.edu/datasets-2/datasets/>.

445 3.4.2 Analysis of Sediment Flows in South America

446 A study of QSS patterns was conducted using time series, from the calibrated model. QSS were
447 simulated using the inertial and Muskingum-Cunge routing methods to assess the impact of
448 fluvial hydrodynamics and floodplains on sediment transport and deposition. We also evaluate
449 the effect of calibration and hydrodynamic routing on sediment delivery to the Oceans. For this
450 purpose, we compared the estimated loads from a simulation considering hydrodynamic routing
451 without calibration (i.e., setting the values 11.8 and 0.56 for parameters α and β , respectively)
452 versus simulations using the inertial and Muskingum-Cunge methods to estimated loads
453 considering the calibrated model.

454 To understand the spatial dynamics of the sediment flows in the SA, long-term averages of SSC,
455 denudation rate, deposition of suspended sediment in the floodplains, and water discharge were
456 calculated. We identified the major floodplains where the highest deposition rates occur, but the
457 results were only presented for those basins where the model was calibrated, i.e., where there
458 was no transfer of parameters, as in the case of the Orinoco River basin. We also computed the
459 annual sediment balance at the outlets of the large rivers and for the whole SA.

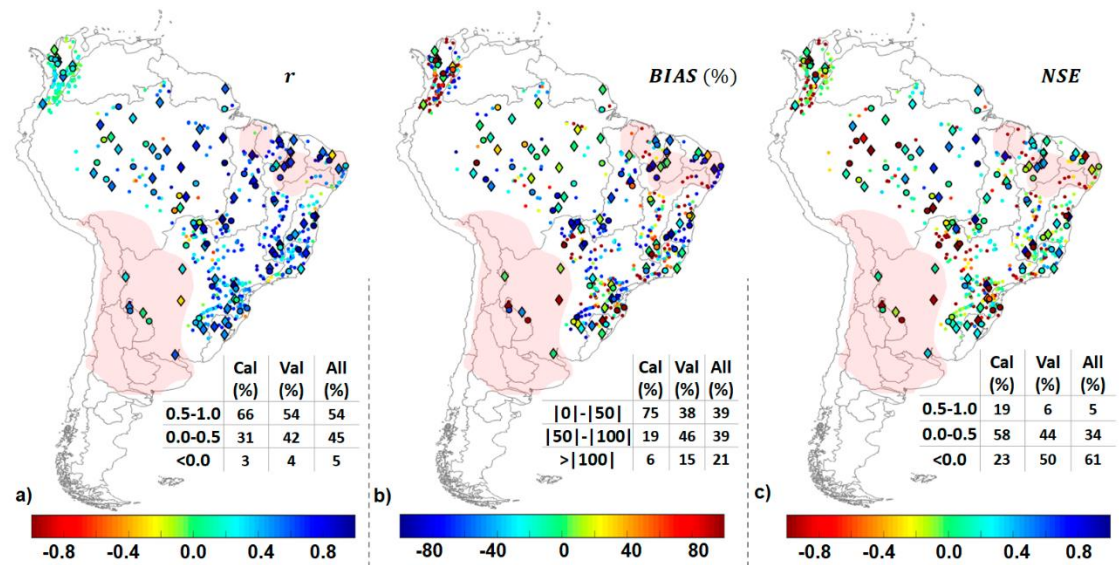
460 4 Results and Discussions

461 4.1 Model Validation

462 4.1.1 Simulated data vs. in-situ observations

463 The mass balance analysis (Table 3, supplementary material S2) showed that the MGB-SED AS
464 model remained stable throughout the simulation. Numerical errors were of the $10^{-3}\%$ order,
465 mostly coming from variables truncation in the operations.

466 The simulated QSS was compared against observed daily values, and the performance of the
467 model was evaluated in Figure 4 in terms of r , *BIAS* and *NSE*. Other metrics are shown in
468 Figure 2 of the supplementary material S2.

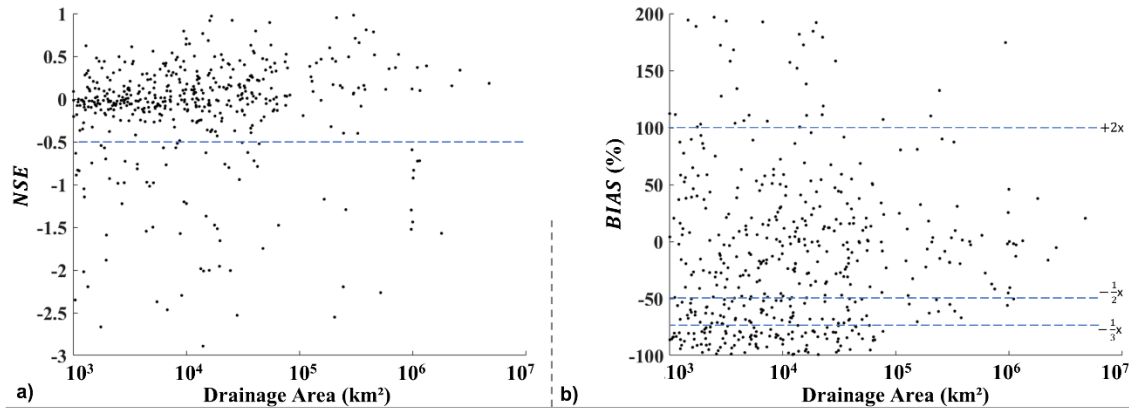


469

470 **Figure 4:** MGB-SED AS performance over South America in terms of suspended sediment discharge: a) correlation
 471 (r); b) $BIAS$ (%); and c) Nash-Sutcliffe efficiency (NSE). Diamonds and bigger dots refer to stations used in
 472 calibrating (Cal) and validating (Val) steps, respectively. Small dots refer to other station used to evaluate the model.
 473 Tables summarize the percentage of sediment stations in each performance class and corresponding step. Marked
 474 regions represent those with poor hydrological-hydrodynamic performance (see Siqueira et al., 2018).

475 Figure 4-a indicated agreement between model estimates and observed data in terms of
 476 correlation, in which 66% and 54% of the stations had values higher than 0.5 in the calibration
 477 (Cal) and validation (Val) steps, respectively. In terms of $BIAS$, 94% (Cal) and 85% (Val) of the
 478 stations had values between -100% and 100% (Figure 4-b). For NSE , 78% and 50% of the
 479 stations had positive values (Figure 4-c).

480 In the evaluation using all stations (All), Figure 4 shows that MGB-SED AS model had a
 481 lower performance in comparison to calibration and validation. We observed a better model
 482 performance to simulate QSS for stations used in the calibration, and worse model performance
 483 (r , $NSE < 0.0$ and $BIAS > |100|$) was noticed especially in three situations. The first one is related to
 484 the regions where the hydrological model performed poorly (Figure 4), characterized by arid or
 485 semi-arid climate; regions where snow melting plays an important role for the runoff generation;
 486 and regions influenced by orography (Siqueira et al., 2018). The second one is represented by
 487 rivers influenced by the presence of dams, which affect the sediment transport, such as the São
 488 Francisco, Jequitinhonha, Tocantins, Paraná, Salado, Madeira, Parnaíba and Doce rivers (See
 489 Figure 1: South America showing: a) major hydrological regions according to FAO and Agência Nacional de
 490 Águas do Brasil (ANA) classifications, relief map based on the Bare-Earth SRTM (O'Loughlin et al., 2016),
 491 including main rivers, flooded areas (Fluet-Chouinard et al., 2015) and artificial lakes (Lehner et al., 2011); and b)
 492 existent dams from GRanD v1.3 product ($>0.1 \text{ km}^3$ Lehner et al., 2011 - <http://globaldamwatch.org>) and from ANA
 493 ($> 30\text{MW}$), and sediment stations from ANA, Base de Datos Hidrológica Integrada da Argentina (BDHI) and
 494 Instituto de Hidrologia, Meteorología e Estudos Ambientais da Colômbia (IDEAM). and Figure 4). The third
 495 one is for the stations having small drainage areas. For the latter situation, Figure 5 presents a
 496 detailed description of the modeling results that relate the drainage area of each station to the
 497 NSE and $BIAS$ values. It is noted that for areas larger than $100,000\text{km}^2$, the $BIAS$ range is
 498 reduced (values between -67% and 200%), remaining mostly between -50 and 50% (Figure 5-b).
 499 For the NSE , most values are over -0.5 (Figure 5-a).



500

501 **Figure 5:** *NSE* and *BIAS* (%) between observed and simulated QSS compared against the drainage area.
 502 Dashed blue lines in b) represent how much MGB-SED AS model over or underestimate QSS values.

503 Many stations that have small drainage areas are found in Colombia, for example. The results of
 504 Figure 4 in this region do not show a specific pattern, and the *NSE* and *BIAS* values are
 505 sometimes negative, sometimes positive. These basins also have high slope values and are
 506 characterized by the occurrence of strong storms (Restrepo et al., 2006). The resolution of the
 507 models input data and the computational resources generally available difficult the representation
 508 of these features in continental-scale models.

509 In Table 4 of the supplementary material S2, we present an analysis of the model performance
 510 for several stations and the period when the model was calibrated (2002-2009) and the non-
 511 calibrated (1992-2001). The analysis shows that temporal extrapolation performed better than
 512 spatial extrapolation. The temporal extrapolation refers to the model evaluation for calibrated
 513 stations in another period. Spatial extrapolation refers to the model evaluation in the same period
 514 as the calibration, but for stations not used in that process.

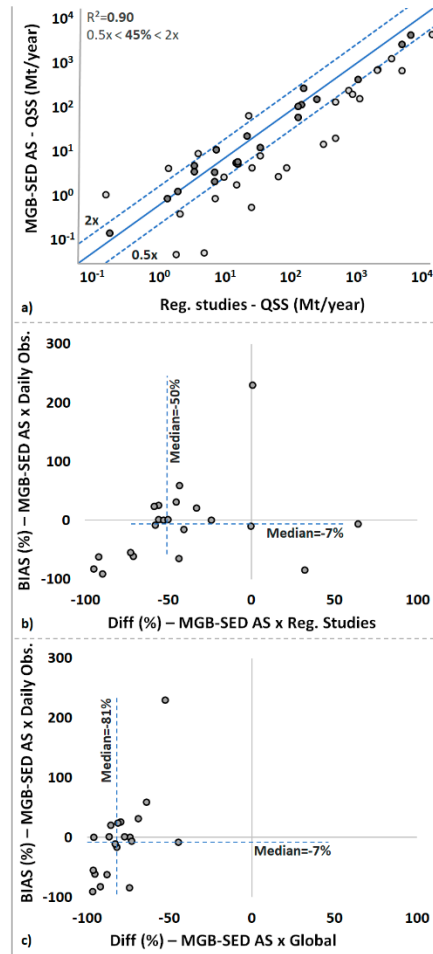
515 4.1.2 Simulated data vs. other studies

516 The comparison between simulated annual QSS and estimated annual QSS by regional
 517 studies showed an $R^2=0.90$ (Figure 6-a). 45% of comparisons revealed that the MGB-SED AS
 518 estimates range between half and twice the values found in regional studies.

519 Figure 6-a also shows a trend for MGB-SED AS QSS to be lower than the regional
 520 studies QSS. Figure 6-b presents a comparison of *BIAS* (MGB-SED SA and in-situ measured
 521 data) versus *Diff* (MGB-SED SA and regional studies). The results indicate that the *BIAS* and
 522 *Diff* median were, respectively, -7% and -50%.

523 To understand the differences presented in the previous paragraph, we highlight that: i)
 524 the medians of *BIAS* and *NSE* were, respectively, -7% and 0.13 for the 21 analyzed stations; ii)
 525 in the Fazenda Vista Alegre station, for example, the daily *BIAS* and *NSE* were, respectively,
 526 1% and 0.39, but in comparison with Lima et al. (2005) study, the MGB-SED AS has estimated
 527 for this station QSS values 56% lower; iii) the Lima et al. (2005), Latrubesse et al. (2005) and
 528 Restrepo et al. (2006) studies provided estimates using regression methods between QSS and
 529 water discharges. From the three points presented, we realize that MGB-SED AS had better
 530 agreement with in-situ data than with estimated data from regional studies. Besides, the
 531 regression methods used in the aforementioned studies are simplified, and they consider some

532 assumptions that may increase their estimates, such as: the use of few in-situ measured data, in
 533 which the majority belonging to the low-concentration period, to represent the temporal
 534 dynamics of sediments; Q enough to explain QSS; the increase of QSS is always increasing with
 535 Q. However, because of hysteresis effects, it is known that these premises often do not occur in
 536 nature, especially for large rivers, which is clearly demonstrated for the Amazon in studies
 537 performed by Bourgoin et al. (2007), Filizola et al. (2011) e Fassoni-Andrade and Paiva (2019).
 538 A broader discussion on this topic is presented in the next section.



539

540 **Figure 6:** Performance of the MGB-SED AS model against the results of regional and global studies. a) comparison
 541 between MGB-SED AS annual suspended sediment discharge (QSS) and QSS from regional studies; light gray dots
 542 refer to when the MGB-SED AS estimated more than double or less than half the regional studies values. b)
 543 comparison between MGB-SED AS and QSS in-situ daily observations (*BIAS*) against MGB-SED AS and annual
 544 QSS from regional studies (*Diff*). c) comparison between MGB-SED AS and QSS in-situ daily observations
 545 against MGB-SED AS and annual QSS from the WBMsed global model (Cohen et al., 2014), using *BIAS* and
 546 *Diff*, respectively.

547 Figure 6-c presents a comparison between the results of MGB-SED AS and those of the
 548 WBMsed global model (Cohen et al., 2014). The median *Diff* between the MGB-SED AS and
 549 the WBMsed model was -81%, and the highest value was -44%. It shows that the estimated
 550 values by MGB-SED SA are considerably lower than those predicted by WBMsed. In this case,
 551 although the WBMsed model does not consider the only Q to estimate QSS, it is based on a

552 global empirical equation, which may have limitations given the different variables around the
553 globe. The WBMsed model was neither calibrated nor validated by Cohen et al. (2014) in SA.

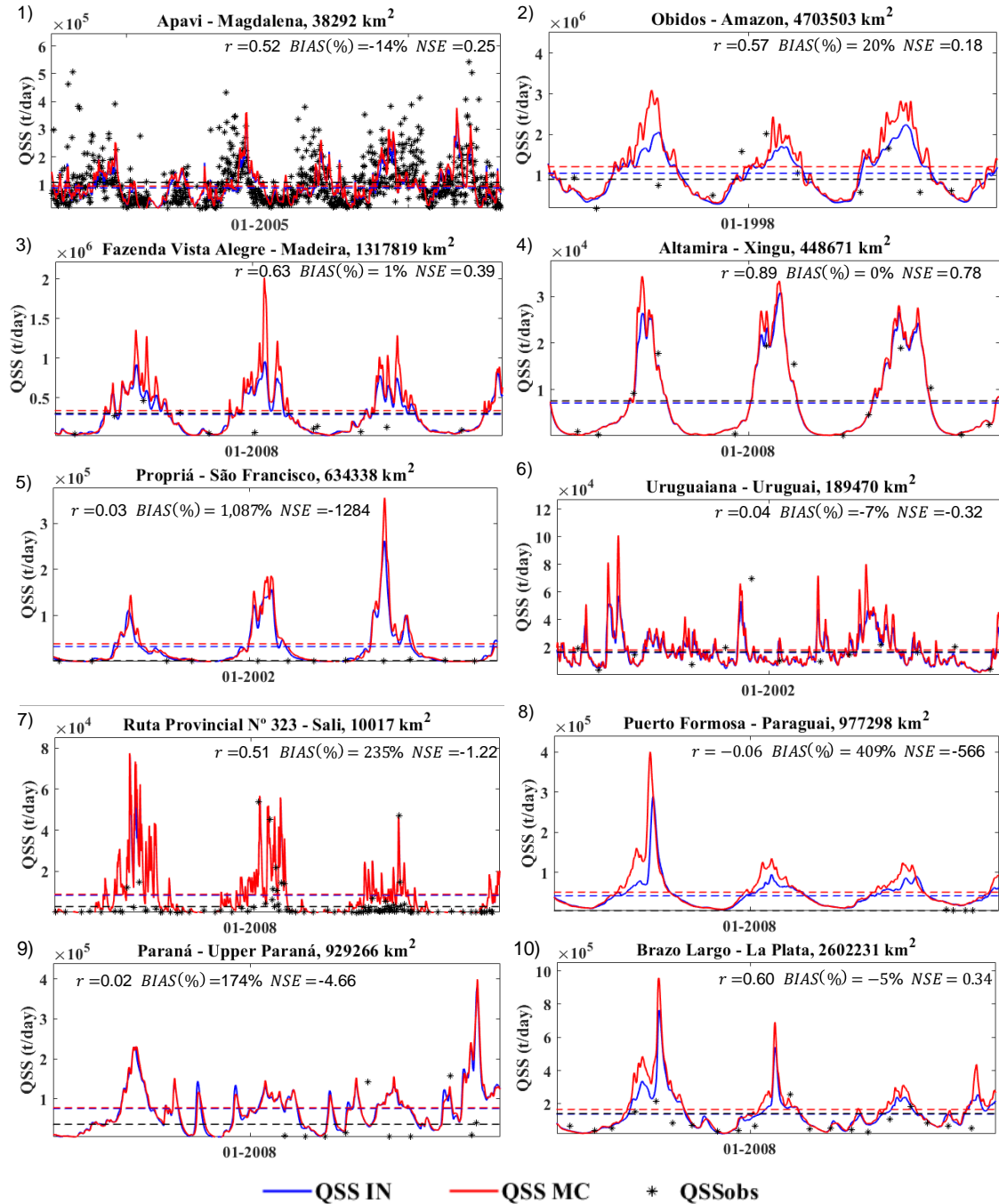
554 The tables used to generate Figure 6 graphics can be found on the supplementary material
555 S2 (Table 1 and Table2).

556 4.2 Analysis of Sediment Flows in South America

557 4.2.1 Time Series

558 Figure 7 presents the comparison between daily simulated and in-situ QSS data for
559 several large South American rivers. The presented statistics were calculated considering only
560 the values of observation dates. Apavi station, on the Magdalena river (Figure 7-1), offers a lot
561 of observed data, and, in general, there was an agreement between the simulated and observed
562 data ($BIAS=-14\%$ and $NSE=0.25$). In the Amazon basin, suspended sediments were well
563 represented for several stations, which can be seen in the Óbidos (Figure 7-2), Fazenda Vista
564 Alegre (Figure 7-3) and Altamira (Figure 7-3) stations. The latter had $BIAS=0\%$ and $NSE=0.78$.
565 It is pointed out that the variability of the QSS estimated by the sediment model is strongly
566 influenced by the variability of hydrological variables calculated by MGB AS.

567 The impact of fluvial hydrodynamics on sediment transport can be observed at Fazenda
568 Vista Alegre and Óbidos stations, where the floodplains act storing sediments and, consequently,
569 reducing the peaks of QSS ($QSS_{MC} > QSS_{IN}$). In other places, the effect of hydrodynamic
570 routing is less significant, as in the Propriá (Figure 7-5) and Paraná (Figure 7-9) stations, the
571 QSS MC and QSS IN curves are closest, differing only at the highest points. These are usually
572 regions where the presence of floodplains is less expressive, and the average slopes of the rivers
573 are higher.



574

575 **Figure 7:** Comparison between observed (QSSobs - black asterisks) and simulated suspended sediment discharge
 576 (QSS) for some large rivers of South America. Model performance is presented in terms of correlation (r),
 577 $BIAS$ (%) and Nash-Sutcliffe efficiency (NSE) for hydrodynamic modeling (QSS IN). Daily QSS simulated time series
 578 are presented for both inertial (QSS IN - blue lines) and Muskingum-Cunge (QSS MC – red lines) routing
 579 methods. Dashed lines show the respective long term averages. The sediment stations locations are presented in
 580 Figure 8-a.

581 In the Propriá station, the $BIAS$ was 1,087%, and in-situ QSS values were always very
 582 low (Figure 7-5). In this case, as for other stations like Paraná (Figure 7-9), these low observed
 583 values are associated with sediment trap in large dams located upstream. Highlighting this

584 phenomenon is important because, in these cases, the observed temporal dynamics are
585 inconsistent with the simulated natural sediment discharge in the rivers.

586 The Puerto Formosa station (Figure 7-8), in the Paraguay River, also showed low
587 performance, which can be related to the weak performance of the MGB AS model in the
588 upstream drained region. Also, this region is strongly influenced by the Pantanal wetlands, where
589 a complex rivers network having bifurcations and diffuse flows in the floodplains are noted,
590 which are not well represented by one-dimensional models, such as the MGB AS. The low
591 performance may also be related to the lack of in-situ data (only 4 in total), which compromises a
592 proper comparison between simulated and observed data. Despite the low performance of the
593 hydrological model in a large area of the La Plata river basin and the several impoundments in
594 the Paraná River, the model presented a *BIAS* of -5% and an *NSE* of 0.34 at the outlet of the La
595 Plata River (Figure 7-10).

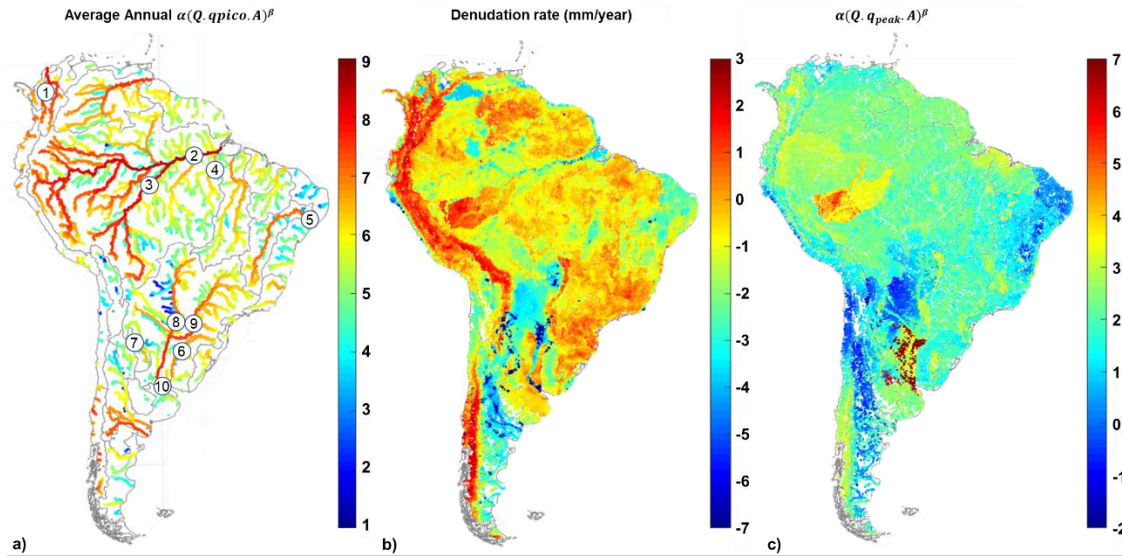
596 In many places, the model estimates and in-situ observations did not match, which may
597 have been caused by the non-representation of reservoirs in the modeling process. In the São
598 Francisco River, sediment trapped by reservoirs may approach 70% (Creech et al., 2015).
599 Syvitski et al. (2005), considering impoundments, estimated that sediment flows to the oceans in
600 SA were reduced by about 13%/ year. The expectation of the construction of new dams in the SA
601 and their impacts on water and sediment flows, mainly in the Amazon Basin (Latrubesse et al.,
602 2017), have grown. So, it is crucial to consider these structures in simulations aiming to quantify
603 sediment flows in the present and future scenarios.

604 4.2.2 Spatial Analysis

605 Figure 8-a presents the long-term average annual QSS (t/year). From the simulated
606 results, the Amazon River is the one with the highest QSS (3.89×10^8 t/year), followed by the
607 Magdalena (7.57×10^7 t/year) and La Plata (5.07×10^7 t/year) rivers. The Magdalena carries a load
608 six and ten times greater than those carried by the São Francisco (1.20×10^7 t/year) and Tocantins
609 (7.29×10^7 t/year) rivers, which have twice their drainage area. The average flows of the São
610 Francisco and Tocantins rivers are 56% lower and 88% higher, respectively, than the Magdalena
611 river. The Doce River transports a suspended load of 4.81×10^6 t/year, which is equivalent to 40%
612 of the load carried by the Tocantins River, although the Doce River has a drainage area (flow)
613 ten (fourteen) times smaller.

614 A QSS value of 3.77×10^7 t/year was estimated for the Orinoco river, a value almost five
615 times lower than that (15.0×10^7 t/year) estimated by Latrubesse et al. (2005). The Orinoco river
616 basin was not calibrated, as we did not have stations with data observed in this region. The
617 comparison of annual QSS values with estimates made by regional studies is presented in
618 supplementary material S2.

619 The simulated QSS for the most downstream stations of each basin agreed with the
620 observed values (*BIAS* values, Figure 4), which allows us to make more accurate estimates, from
621 our perspective, of the natural loads reaching the oceans. Thus, Figure 8-a represents a potential
622 transport situation in the rivers since a sediment trapping in dams was not considered in the
623 sediment modeling. Rivers such as the São Francisco and Paraná, for example, currently have
624 clearer waters downstream from the dams.



625
 626 **Figure 8:** Average Annual a) suspended sediment discharge (QSS) over South America; b) denudation rate
 627 (silt+clay+sand); and c) $\alpha(Q \cdot q_{peak} \cdot A)^\beta$. Colorbar values are in the logarithmic scale. Numbers in c) refer to
 628 stations showed in Figure 7.

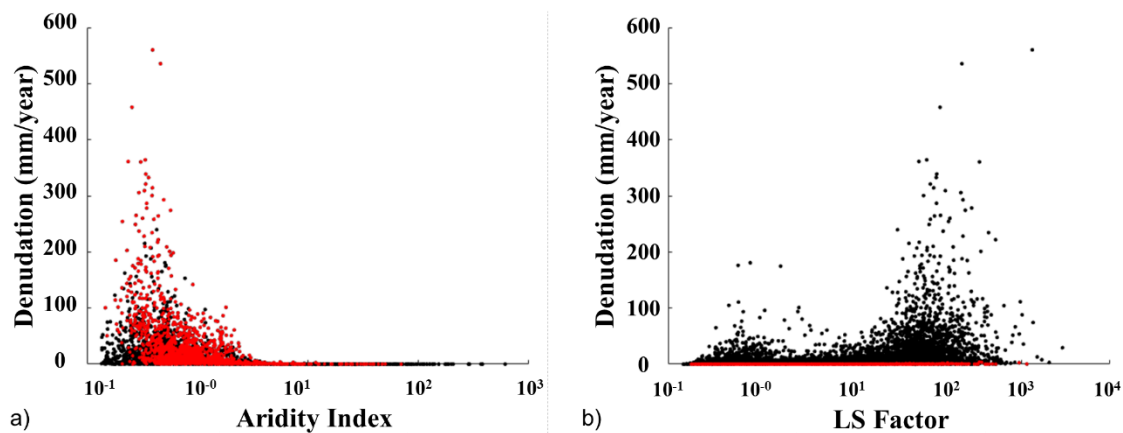
629 Figure 8-b shows spatial patterns of denudation rates (soil loss in mm/year; sediment
 630 density equal to 2.65 t/m³ was used for the unit conversion, see Morris and Fan, 1998). The SA
 631 average value is 2.90 mm/year. With 16.67 mm/year, the Magdalena basin presented the highest
 632 mean denudation rate. The Amazon basin had the second-highest denudation rate of 3.35
 633 mm/year. In the Juruá, Solimões and Madeira river basins, denudation rate was 8.58, 6.28 and
 634 3.70 mm/year, respectively. For the Negro, Tapajós and Xingu watersheds, these values were
 635 0.41, 0.40 and 0.28, respectively. While we found a 0.41 mm/year, Wittmann et al. (2011) found
 636 a denudation rate ten times lower for the Negro River through estimates based on cosmogenic
 637 nuclides of Beryllium and Aluminium.

638 The high denudation rates calculated for the Magdalena and Amazon river basins are
 639 mainly associated with the high slopes and strong storm events in the Andean region (see Guyot
 640 et al., 1996; Restrepo et al., 2006). The Restrepo et al. (2006) analysis, between 1986 and 1996
 641 using more than 30 stations, indicated an increasing trend of erosion in the Magdalena basin.
 642 Among the causes for this increase are catchments with small drainage areas having high relief
 643 and narrow alluvial plains, heavy precipitations, and changes in land use and land cover.
 644 Furthermore, compared to the Amazon, the Magdalena basin is more influenced by the Andes
 645 and has fewer flat regions (Figure 1: South America showing: a) major hydrological regions according to
 646 FAO and Agência Nacional de Águas do Brasil (ANA) classifications, relief map based on the Bare-Earth SRTM
 647 (O'Loughlin et al., 2016), including main rivers, flooded areas (Fluet-Chouinard et al., 2015) and artificial lakes
 648 (Lehner et al., 2011); and b) existent dams from GRanD v1.3 product (>0.1 km³ Lehner et al., 2011 -
 649 <http://globaldamwatch.org>) and from ANA (> 30MW), and sediment stations from ANA, Base de Datos
 650 Hidrológica Integrada da Argentina (BDHI) and Instituto de Hidrologia, Meteorologia e Estudos Ambientais da
 651 Colômbia (IDEAM).).

652 The Doce and the Paraná river basins also stand out with high denudation rates: 2.12
 653 mm/year and 1.31 mm/year, respectively. These basins have a strongly undulating and hilly
 654 relief, soils covered mainly by agriculture and degraded pastures, and a very seasonal rainfall
 655 pattern, with heavy rainfall for the November-January period. Despite the Parnaíba and São

656 Francisco river basins having a hilly relief, they are in a semi-arid region, for which lower
 657 denudation rates are estimated (0.28 mm/year and 0.85 mm/year, respectively).

658 The relations between denudation rate, slope (represented by the *LS* factor), and
 659 precipitation (represented by the Aridity index) are presented in Figure 9. This figure shows, in
 660 agreement with Figure 3 and Figure 8, that high denudation rates can occur for high and low
 661 slopes, and are found mainly in humid areas (Aridity Index <100, Figure 9-a), but arid regions
 662 always have very low denudation rates (Figure 9-b). Figure 9 shows that a pattern between the
 663 denudation rate, *LS* factor and aridity index does not exist. We expected this, since the model
 664 considers several processes based on what occurs in nature, and not only the water discharge, to
 665 estimate erosion and sediment transport. García-Ruiz et al. (2015) identified, from several
 666 studies around the world, that almost all erosion rates can occur for any climate condition. The
 667 authors also pointed out that a significant effect of the increase in erosion rates occurs as
 668 precipitation and slope rise. This increase tends to reach, on average, a limit when the slope and
 669 precipitation reach $\pm 0.2\text{m/m}$ and $\pm 1,400\text{mm/year}$, respectively.



670
 671 **Figure 9:** Denudation rate versus: a) Aridity Index (red dots represent *LS* values above the percentile 95%); b) *LS*
 672 factor (red dots represent Aridity Index values above the percentile 95%).

673 The MUSLE factor related to the ability to remove soil particles is the $\alpha(Q \cdot q_{peak} \cdot A)\beta$.
 674 In regions such as Brazilian northeast, Chaco, Atacama Desert, and others in the south of the
 675 continent (Desaguadero, Colorado and Negro river basins), the values of this factor are
 676 comparatively low concerning the rest of the SA. High values are found in the Purus River basin,
 677 part of the Juruá River basin, and in the lower La Plata river basin (Figure 8-c). It is noticeable
 678 that some spatial patterns presented in Figure 8-b are directly related to the standards presented
 679 in Figure 8-c, showing the influence of the $\alpha(Q \cdot q_{peak} \cdot A)\beta$ factor in the denudation rate.

680 In the Purus River, even the $\alpha(Q \cdot q_{peak} \cdot A)\beta$ factor values being higher, the simulated
 681 QSS tended to underestimate the observed values (Figure 4). Thus, we believe that these
 682 highlighted values may be related to the calibration parameters of the hydrological model and the
 683 spatial discretization performed by Siqueira et al. (2018), which was more focused on
 684 hydrological processes than sediment processes. Also, no pattern was observed in the maps of
 685 the input parameters (Figure 3) that could explain the observed pattern for the Purus and Juruá
 686 river basins in Figure 8-b. The reach of the lower La Plata river was calibrated using a station
 687 that is affected by the sediment trap in the Paraná River dams. This effect may have led the

688 optimization algorithm to compensate for the sediment supply by increasing the values of the
689 $\alpha(Q \cdot q_{peak} \cdot A)^\beta$ factor in this region.

690 4.2.3 Multiple relationships: water discharge, sediment concentration and deposition

691 4.2.3.1 Overview

692 Figure 10 shows SA rivers with the highest Q and SSC values according to the modeling
693 results. The figure illustrates that largest SSC values in the Amazon basin are located in the
694 upper Madeira River and other rivers having the headwaters in Andean regions, as already
695 known by previous studies (Amsler and Drago, 2009; Cohen et al., 2014; Latrubesse et al.,
696 2005). The pattern found in the river reaches with higher and lower concentrations in the central
697 Amazon matches well with the results found by Fassoni-Andrade and Paiva (2019) using remote
698 sensing. The greatest differences are found downstream of the confluence between the Amazon
699 and Tapajós rivers, where the SSC (Figure 10) keeps decreasing, while Fassoni-Andrade and
700 Paiva (2019) observed an increase downstream of the confluence with the Xingú River. The
701 authors concluded that this difference could be associated with sediment resuspension caused by
702 variations at the Amazon estuary, which are not represented in the MGB-SED AS model.

703 The Magdalena, Pilcomayo, and some rivers in the south of SA (Negro and Desaguadero)
704 showed high concentrations, but only Magdalena can be calibrated and validated. The
705 Amazonian rivers without headwaters in the Andes have low SSC, such as the Negro, Tapajós
706 and Xingu rivers (Figure 10), having high water discharge values ($>9,700 \text{ m}^3/\text{s}$ in average, see
707 Latrubesse et al., 2005).

708 It was estimated that 1.17×10^9 t/year of suspended sediment (SS) arrived in SA rivers
709 under natural conditions (i.e., without impoundments). Of these, about 1.11×10^8 t/year (9.4%)
710 are trapped in the floodplains before reaching the Oceans.

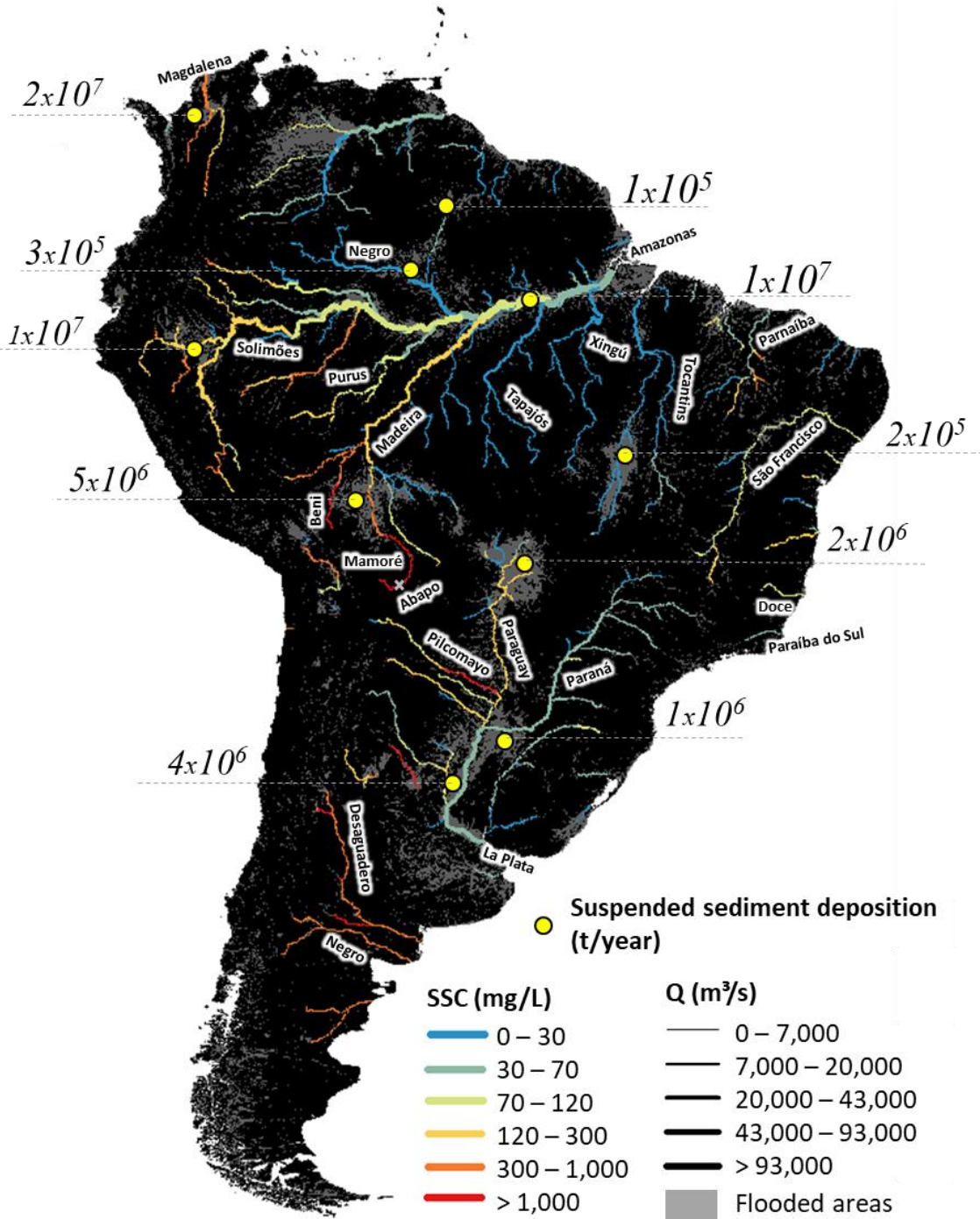
711 The effect of SS deposition on the floodplains is quite evident in the highlands of the
712 Madeira river basin (Figure 10), causing a sharp reduction in SSC values from upstream to
713 downstream. For example, Guyot et al. (1996), using regressions between observed Q and QSS
714 data, estimated a 43% and 63% reduction in QSS and SSC values, respectively, at two points on
715 the Beni River. Taking the same locations as a reference, we estimated that there was a 10%
716 (58%) increase (decrease) in simulated QSS (SSC). In Mamoré River, the authors used the same
717 approach and also estimated a reduction for QSS and SSC of 54% and 95%, respectively. In
718 comparison, we estimated a 34% (76%) increase (decrease) for QSS (SSC).

719 The region assessed on the Mamoré River drains a large amount of sediment originating
720 in the Andes. The same happens with the Pilcomayo River. The Mamoré River flows through
721 regions with dynamic and complex fluvial geomorphology, with avulsion and silting
722 mechanisms of the bed in the Llanos de Moxos floodplain. It was estimated that about 5×10^6
723 t/year of SS are deposited in this floodplain (Figure 10). The Pilcomayo River flows through and
724 floods the flat regions of the Chaco, losing water to the atmosphere through evapotranspiration
725 (Martín-Vide et al., 2014). The Pilcomayo River basin also presents great complexities, similar
726 to those described for the Mamoré River (see Martín-Vide et al., 2014). In the upper Pilcomayo,
727 near the Andes, Martín-Vide et al. (2014) estimated a mean SSC of $15 \times 10^3 \text{ mg/L}$, while SSC
728 simulated was 168 mg/L , about 100 times lower. Guyot et al. (1996) estimated a mean SSC of
729 $13 \times 10^3 \text{ mg/L}$ in Abapo (Figure 10), about six times higher than estimated with MGB-SED AS

730 (2×10^3 mg/L) and a bit more than double estimated by Buarque (2015), in which it was found
 731 5×10^3 mg/L (personal communication) using a regional model.

732

733



734

735 **Figure 10:** Annual average of suspended sediment load deposited in the main floodplains of South America; long-
 736 term daily average of suspended sediment concentration (SSC) and water discharge (Q) for main large rivers.
 737 Flooded areas were acquired from Fluet-Chouinard et al. (2015).

738 Therefore it is possible to notice that MGB-SED SA has estimated lower SSC values in
739 the Mamoré and upper Pilcomayo rivers as we compare to studies made by Guyot et al. (1996)
740 and Martín-Vide et al. (2014), respectively. The main differences found could be related to the
741 following aspects: i) there was difficulty in calibrating the continental-scale model in the regions
742 of upper Madeira and upper Pilcomayo, with the available data; ii) the processes observed in the
743 Andean region, such as landslide-driven sediment flux, are not well represented in the proposed
744 modeling as discussed by Buarque (2015), which shows that significant uncertainties for these
745 regions may exist. As the model shows lower estimates of SSC in these two areas, the deposition
746 values are possibly higher than those estimated.

747 The Pilcomayo River was the only river that showed an increase in concentrations from
748 upstream to downstream (Figure 10). It happens because simulated Q values increase from the
749 upstream to the middle Pilcomayo and decrease again next to the outlet. Martín-Vide et al.
750 (2014) noted that the increase in Q is not proportional to the SSC for the Pilcomayo River. This
751 behavior was identified using MGB-SED AS for the Mamoré River, which differs from the
752 approach used by Guyot et al. (1996). Using the MGB-SED model, which considers several
753 processes and variables and not only Q to estimate the QSS, Buarque (2015) found a $NSE=0.7$
754 in the Fazenda Vista Alegre station (Madeira River). This indicates that the connection suggested
755 in some studies (e.g., Guyot et al., 1996; Latrubesse et al., 2005; Lima et al., 2005; Restrepo et
756 al., 2006), that QSS always increases with Q, cannot always be applied.

757 The assessment in large flooded areas (Figure 10) indicated that 53% (5.26×10^7 t/year) of
758 SS is deposited in them. The three plains having the highest amounts of deposited SS are the
759 Magdalena Delta (2×10^7 t/year), central Amazon floodplains (1×10^7 t/year) and the interfluvial
760 floodplains of Peru (1×10^7 t/year). In the whole Amazon basin, about 2.54×10^7 t/year of SS are
761 deposited in floodplains (Figure 10). All other floodplains outside the Amazon and Magdalena
762 river basins retain annually 7.2×10^6 tones (Figure 10).

763 4.2.3.2 Annual Sediment Balance

764 The impact of model calibration and hydrodynamic routing in South America was also
765 assessed by the suspended loads leaving the continent. When using the hydrodynamic model
766 without calibration, the QSS reaching the oceans was 2.86×10^9 t/year. After calibration, this
767 value was 1.00×10^9 t/year, which means that the calibration of MGB-SED AS provided
768 estimates 65% lower. When the calibration and Muskingum-Cunge routing method were
769 considered, the value increased by 12% (1.12×10^9 t/year). Syvitski et al. (2005) estimated for
770 "prehuman" period that QSS delivered from SA was, on average 2.68×10^9 t/year, a value 268%
771 (6%) higher (lower) than estimated with calibrated (non-calibrated) MGB-SED AS. In their
772 global study on tropical rivers, Syvitski et al. (2014) highlighted that most modeling projects use
773 boundary conditions without considering sediment depositions in the deltas, which could reduce
774 the value of the SS that effectively leaves the continent. In this paper, we partially represent this
775 effect, since the model does not consider coastal basins and islands with $A < 1,000 \text{ km}^2$ or
776 submerged coastal regions.

777 Naturally (without considering impoundments), the daily water (SS) transport of
778 $3.10 \times 10^{10} \text{ m}^3$ (2.76×10^6 t) by the SA rivers to the oceans was estimated using MGB-SED AS. Of
779 this total, 57% (39%) of the water (SS) volume comes from the Amazon basin.

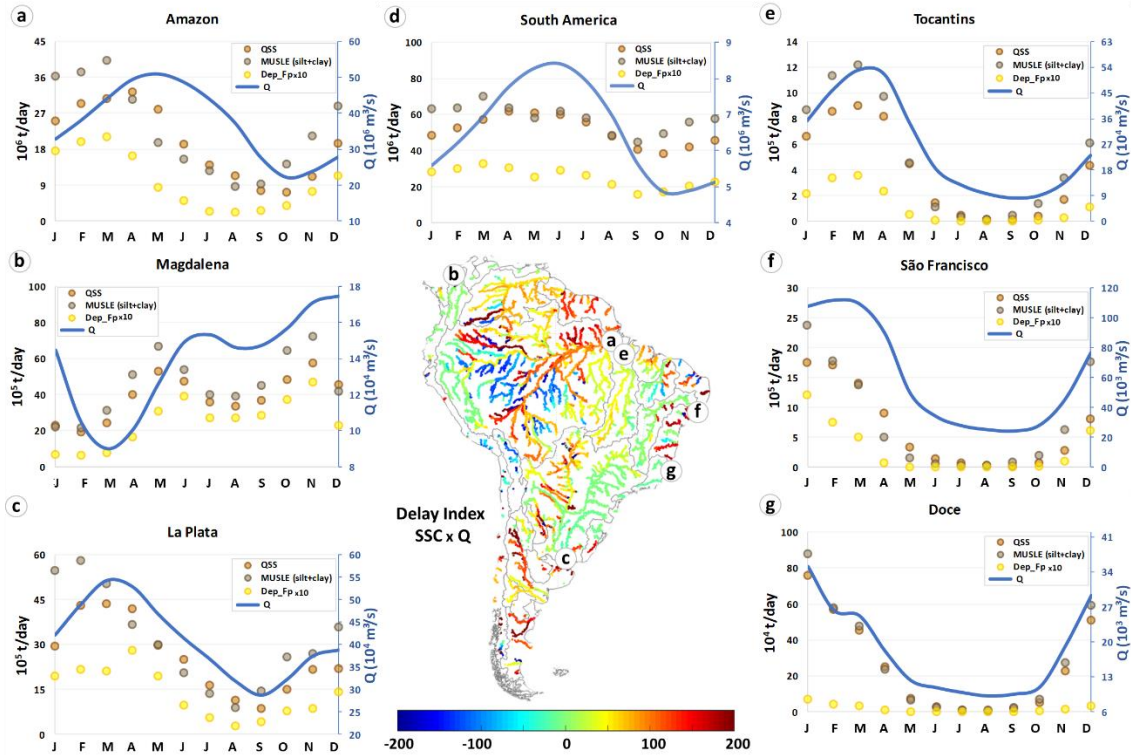
780 Figure 11 presents a monthly balance of SS and Q for South America and several of its
781 major rivers. In addition, to expand the understanding of the different relations between Q and
782 SSC, a map with the Delay Index (*DI*) calculated between these two variables is also presented
783 in this figure. Values in red (blue) shades show how many days the SSC peak is ahead (behind)
784 in relation to the Q peak.

785 The *DI* map (Figure 11) shows that, especially in flat regions, the SSC peak in rivers
786 occurs earlier than the Q peak. In the Magdalena River, *DI* values become higher in and after
787 crossing floodplains. In Figure 11-a and Figure 11-b, the occurrence of the QSS peak before the
788 Q peak is also observed. This information again suggests that expressing the QSS increase as a
789 function of Q, from a regression with an always increasing curve, may not be adequate in all
790 cases. Figure 11 map also shows that in some places, as in the flatter regions of the Amazon
791 basin, negative values of *DI* occur. For several of these regions the simulated SSC had very low
792 values (<10mg/L, Figure 10), which decrease even more in high flow periods. For these places,
793 water volumes dominate the SSC values, with a higher or lower dilution of the SS loads. In the
794 Paraná, São Francisco, Upper Paraguay, Doce, and Paraíba do Sul river basins, *DI* values are
795 closer to zero. A common feature of these basins is that they have hilly relief regions and few flat
796 areas, facilitating the water and sediment transport. Most of these basins also have a well-defined
797 seasonal precipitation pattern, raining heavily in the summer.

798 Throughout the year, the simulated QSS in AS ranged $40\text{-}60 \times 10^6$ t/day, in which higher
799 values were occurring between February and July (Figure 11-d). The SS deposition on the
800 floodplains has higher values between January and June.

801 In the Amazon River, the sediment supply (MUSLE) peak was in March, together with
802 the floodplains deposition (Dep_{fp}) peak, and the QSS peak only occurs in April (Figure 11-a).
803 The Amazon River dynamics is mainly influenced by lateral contributions, which is related to
804 the variation of the rainy periods in the south and north of the basin (Villar et al., 2008). In the
805 south, there is the Madeira River basin with high sediment yield (27% of all Amazonas) and the
806 occurrence of QSS and Q peaks, respectively, in January and April. In the north, there is the
807 Negro River with low sediment yield (2.5% of all Amazonas) and the occurrence of QSS and Q
808 peaks, respectively, in June and July. The Solimões River is the one that, in fact, determines the
809 standards of the Amazon River, delivering 65%, on average, of the Amazon SS load upstream of
810 the confluence with the Purus River. In this place, the QSS peak occurs in April, and the peak of
811 the sediment supply and deposition in the floodplains occurs concomitantly in March.

812 The Magdalena River showed two Q and two QSS peaks (Figure 11-b), where the first peaks are
813 about two months apart (May-July) and the last in about one month (November-December). The
814 two peaks of SS deposition on floodplains occur in June, between the first QSS and Q peaks, and
815 in November, concomitantly with Q and QSS peaks. In the La Plata River, the Q and QSS peaks
816 were observed in March. The SS supply peak was observed in February, and about 4% of these
817 sediments are then deposited on floodplains, in which the deposition peak occurs in April (Figure
818 11-c).



819

820 **Figure 11:** Annual sediment balance for South America and some large rivers. Figures a-g show water discharge
 821 (Q) in blue lines, suspended sediment load estimated with MUSLE equation in gray circles, suspended sediment
 822 discharge (QSS) in brownish circles, and suspended sediment deposited in floodplains (Dep-fp) in yellow circles.
 823 Dep_fp values are one order below other sediment values, so in the figure, we raised the values tenfold. The central
 824 map shows the Delay Index, calculated between the suspended sediment concentration (SSC) and Q. Reddish (blue)
 825 values show how many days the SSC peak is ahead (delayed) in relation to the Q peak.

826 The Tocantins (Figure 11-e) and São Francisco (Figure 11-f) river basins have a similar area, are
 827 geographic close to each other but have very different sediment flows. The Tocantins River
 828 (Figure 11-e) has a large floodplain on the Araguaia River, while the São Francisco River has
 829 almost no floodplains (Figure 1: South America showing: a) major hydrological regions according to FAO
 830 and Agência Nacional de Águas do Brasil (ANA) classifications, relief map based on the Bare-Earth SRTM
 831 (O'Loughlin et al., 2016), including main rivers, flooded areas (Fluet-Chouinard et al., 2015) and artificial lakes
 832 (Lehner et al., 2011); and b) existent dams from GRanD v1.3 product (>0.1 km³ Lehner et al., 2011 -
 833 <http://globaldamwatch.org>) and from ANA (> 30MW), and sediment stations from ANA, Base de Datos
 834 Hidrológica Integrada da Argentina (BDHI) and Instituto de Hidrologia, Meteorologia e Estudos Ambientais da
 835 Colômbia (IDEAM).). Despite this, the São Francisco river basin has a more deposited SS load than
 836 that of Tocantins. This occurs because the São Francisco transports a larger load with lower
 837 flows, which facilitates deposition and because the Araguaia River has a lower sediment yield in
 838 its headwaters (Figure 8). The SS supply, floodplains deposition and transport occur in January
 839 to the São Francisco and in March to the Tocantins.

840 The Doce River presents a straightforward relationship between water discharge and sediments,
 841 and similar monthly variations (Figure 11-g). The Q and QSS peaks occur in January, and only
 842 about 0.6% of the sediments reaching the drainage network (this value can be zero for dry
 843 season) are deposited in floodplains.

844 Figure 11 shows that in basins with larger flat areas (e.g., Magdalena, Amazonas and La Plata),
 845 the SS supply peak occurs concomitantly with the deposition peak. In the Doce and São

846 Francisco river basins, the SS supply peak occurs together with the deposition and Q peaks. It
847 means that only for the highest flows the SS reach the floodplains of these basins. In the
848 Tocantins river basin, this fact may be related to the low sediment transport in the Araguaia
849 River, which is the main tributary and has the largest flat regions.

850

851

852 **5 Conclusions**

853 In this research, we performed the coupling of the MGB-SED sediment model with the
854 hydrologic-hydrodynamic model of South America (MGB AS). From this coupling, the MGB-
855 SED AS was developed and assessed. Using the model results was possible to investigate and
856 understand temporal and spatial patterns of suspended sediment (SS) flows on a continental
857 scale.

858 The main conclusions related to the process of development, performance evaluation, and
859 application of the model for the comprehension of continental standards are:

- 860 • The MGB-SED AS model was able to perform accurate estimates at several sites, which
861 was evaluated against in-situ measurements. The calibration of the model parameters
862 improved the estimates of the SS flows, obtaining an export value from AS, under natural
863 conditions (without impoundments), equivalent to 65% of the values estimated without
864 calibration.
- 865 • The use of the hydrodynamic routing method enabled better SS estimates, especially the
866 simulated QSS peaks in places having floodplains. By using the simplified routing
867 method and without floodplains, estimates of annual loads have increased by 12%.
- 868 • We observed that the MGB-SED AS results agreed with in-situ observed QSS. The
869 model tends to estimate QSS values smaller than with the estimates from regional studies
870 and the global model used as comparison. The use of the continental model does not
871 exclude the use of models at regional and local scales for smaller-scale studies.
- 872 • The Amazon (3.89×10^8 t/year), Magdalena (7.57×10^7 t/year) and La Plata (5.07×10^7
873 t/year) rivers presented the highest suspended sediment yield, meaning 39%, 8% and 5%
874 of total South America discharges values to the ocean.
- 875 • Floodplains play an important role by retaining about 9.4% (1.11×10^8 t/year) of SS
876 carried by the rivers. About 53% of the total deposition occurs in large flooded areas, for
877 which the Magdalena Delta (2×10^7 t/year), central Amazon floodplains (1×10^7 t/year) and
878 the interfluvial floodplains of Peru (1×10^7 t/year) representing the three regions with the
879 highest deposition rates.
- 880 • The increase in Q does not always result in an increase in SSC/QSS. Especially in rivers
881 with large floodplains, Q and SSC/QSS peaks can occur up to months apart.
- 882 • Catchments with higher slopes and higher rainfall have higher SSC, while QSS tends to
883 be higher where flows are higher.

884 Results presented in this work enabled the comprehension of the spatiotemporal dynamics of SS
885 flows in South America. Generated maps present the annual rates of denudation, transport
886 (discharge and concentration), and deposition (in the plains) of SS throughout the continent.
887 Charts of the annual sediment balance were also generated for some rivers chosen as having high

888 sediment transport. These information may be useful for other studies on a continental scale, for
 889 example, related to reservoirs, fish productivity, nutrient transport, carbon balance, and other
 890 studies related to ecosystem maintenance and soil conservation. Besides, this information can
 891 support decision making, planning, and management of continental land use. Studies such as that
 892 of Latrubesse et al. (2017) have shown a possible increase of dams in South America in the
 893 future. Thus, to have a better knowledge of sediment fluxes in the present, it is necessary to
 894 consider these structures in sediment modeling, which is part of the continuation of this research.

895

896 **Acknowledgments**

897 The first and second authors thanks the Brazilian CNPq (*Conselho Nacional de Desenvolvimento*
 898 *Científico e Tecnológico*) for supporting this research under the Grants Number 167867/2018-0
 899 and 305636/2019-7.

900

901 Datasets for this research are included in this paper: Siqueira et al. (2018).

902 Data supporting this research are available in <http://www.snirh.gov.br/hidroweb/> (ANA),

903 <http://bdhi.hidricosargentina.gob.ar/> (BDHI) e <http://www.ideam.gov.co/> (IDEAM).

904 **References**

- 905 Aguiar, A.P.D., Vieira, I.C.G., Assis, T.O., Dalla-Nora, E.L., Toledo, P.M., Oliveira Santos-
 906 Junior, R.A., Batistella, M., Coelho, A.S., Savaget, E.K., Aragão, L.E.O.C., Nobre, C.A.,
 907 Ometto, J.P.H., 2016. Land use change emission scenarios: Anticipating a forest transition
 908 process in the Brazilian Amazon. *Glob. Chang. Biol.* 22, 1821–1840.
 909 <https://doi.org/10.1111/gcb.13134>
- 910 Alewell, C., Borrelli, P., Meusburger, K., Panagos, P., 2019. Using the USLE: Chances,
 911 challenges and limitations of soil erosion modelling. *Int. Soil Water Conserv. Res.* 7, 203–
 912 225. <https://doi.org/10.1016/j.iswcr.2019.05.004>
- 913 Almagro, A., Oliveira, P.T.S., Nearing, M.A., Hagemann, S., 2017. Projected climate change
 914 impacts in rainfall erosivity over Brazil. *Sci. Rep.* 7, 1–12. <https://doi.org/10.1038/s41598-017-08298-y>
- 916 Almeida, R.M., Tranvik, L., Huszar, V.L.M., Sobek, S., Mendonça, R., Barros, N., Boemer, G.,
 917 Arantes, J.D., J., Roland, F., 2015. Phosphorus transport by the largest Amazon tributary
 918 (Madeira River, Brazil) and its sensitivity to precipitation and damming. *Inl. Waters* 5, 275–
 919 282.
- 920 Amsler, M.L., Drago, E.C., 2009. A review of the suspended sediment budget at the confluence
 921 of the Paran´a and Paraguay Rivers. *Hydrol. Process. An Int. J.* 23, 3230–3235.
 922 <https://doi.org/10.1002/hyp>
- 923 Andreadis, K.M., Schumann, G.J.P., Pavelsky, T., 2013. A simple global river bankfull width
 924 and depth database. *Water Resouces Res.*
- 925 Angarita, H., Wickel, A.J., Sieber, J., Chavarro, J., Maldonado-Ocampo, J.A., Herrera-R, G.A.,
 926 Delgado, J., Purkey, D., 2018. Basin-scale impacts of hydropower development on the
 927 Mompós Depression wetlands, Colombia. *Hydrol. Earth Syst. Sci.* 22, 2839–2865.
 928 <https://doi.org/10.5194/hess-22-2839-2018>
- 929 Aragão, L.E.O.C., 2012. The rainforest ’ s water pump. *Nature* 489, 217–218.
- 930 Arnold, J.G., Srinivasan, R., Muttiah, R.S., Williams, J.R., 1998. Large area hydrologic

- 931 modeling and assessment part I: model development. *J. Am. Water Resour. Assoc.*
932 <https://doi.org/10.1111/j.1752-1688.1998.tb05961.x>
- 933 Bates, P.D., Horritt, M.S., Fewtrell, T.J., 2010. A simple inertial formulation of the shallow
934 water equations for efficient two-dimensional flood inundation modelling. *J. Hydrol.* 387,
935 33–45. <https://doi.org/10.1016/j.jhydrol.2010.03.027>
- 936 Bates, P.D., Neal, J., Sampson, C., Smith, A., Trigg, M., 2018. Progress Toward Hyperresolution
937 Models of Global Flood Hazard. *Risk Model. Hazards Disasters* 211–232.
938 <https://doi.org/doi.org/10.1016/B978-0-12-804071-3.00009-4>
- 939 Beck, H.E., van Dijk, A.I.J.M., de Roo, A., Dutra, E., Fink, G., Orth, R., Schellekens, J., 2017.
940 Global evaluation of runoff from 10 state-of-the-art hydrological models. *Hydrol. Earth*
941 *Syst. Sci.* 21, 2881–2903.
- 942 Beighley, R.E., Gummadi, V., 2011. Developing channel and floodplain dimensions with limited
943 data: A case study in the Amazon Basin. *Earth Surf. Process. Landforms* 36, 1059–1071.
- 944 Benavidez, R., Jackson, B., Maxwell, D., Norton, K., 2018. A review of the (Revised) Universal
945 Soil Loss Equation ((R)USLE): With a view to increasing its global applicability and
946 improving soil loss estimates. *Hydrol. Earth Syst. Sci.* 22, 6059–6086.
947 <https://doi.org/10.5194/hess-22-6059-2018>
- 948 Best, J., 2019. Anthropogenic stresses on the world’s big rivers. *Nat. Geosci.* 12, 7–21.
949 <https://doi.org/10.1038/s41561-018-0262-x>
- 950 Beusen, A.H.W., Dekkers, A.L.M., Bouwman, A.F., Ludwig, W., Harrison, J., 2005. Estimation
951 of global river transport of sediments and associated particulate C, N, and P. *Global*
952 *Biogeochem. Cycles* 19. <https://doi.org/10.1029/2005GB002453>
- 953 Bierkens, M.F.P., 2015. Global hydrology 2015: State, trends, and directions. *Water Resouces*
954 *Res.* 51, 4923–4947. <https://doi.org/10.1002/2015WR017173>.Received
- 955 Borrelli, P., Robinson, D.A., Fleischer, L.R., Lugato, E., Ballabio, C., Alewell, C., Meusburger,
956 K., Modugno, S., Schütt, B., Ferro, V., Bagarello, V., Oost, K. Van, Montanarella, L.,
957 Panagos, P., 2017. An assessment of the global impact of 21st century land use change on
958 soil erosion. *Nat. Commun.* 8, 1–13. <https://doi.org/10.1038/s41467-017-02142-7>
- 959 Bourgoin, L.M., Bonnet, M.P., Martinez, J.M., Kosuth, P., Cochonneau, G., Moreira-Turcq, P.,
960 Guyot, J.L., Vauchel, P., Filizola, N., Seyler, P., 2007. Temporal dynamics of water and
961 sediment exchanges between the Curuaí floodplain and the Amazon River, Brazil. *J.*
962 *Hydrol.* 335, 140–156. <https://doi.org/10.1016/j.jhydrol.2006.11.023>
- 963 Bravo, J.M., Allasia, D., Paz, a. R., Collischonn, W., Tucci, C.E.M., 2012. Coupled Hydrologic-
964 Hydraulic Modeling of the Upper Paraguay River Basin. *J. Hydrol. Eng.* 17, 635–646.
965 [https://doi.org/10.1061/\(ASCE\)HE.1943-5584.0000494](https://doi.org/10.1061/(ASCE)HE.1943-5584.0000494)
- 966 Brêda, J.P.L.F., Paiva, R.C.D., Collischon, W., Bravo, J.M., Siqueira, V.A., Steinke, E.B., 2020.
967 Climate change impacts on South American water balance from a continental-scale
968 hydrological model driven by CMIP5 projections. *Clim. Change.*
969 <https://doi.org/10.1007/s10584-020-02667-9>
- 970 Buarque, D.C., 2015. Simulação da geração e do transporte de sedimetnos em grandes bacias:
971 estudo de caso do rio Madeira. Universidade Federal do Rio Grande do Sul, Porto Alegre,
972 Tese (Doutorado em Recursos Hídricos e Saneamento Ambiental).
- 973 Campagnoli, F., 2006. The production of the sediment of the South America continent: propose
974 of mapping of the erosion rates based on geological and geomorphological aspects. *Rev.*
975 *Bras. Geomorfol.*
- 976 Cohen, S., Kettner, A.J., Syvitski, J.P.M., 2014. Global suspended sediment and water discharge

- 977 dynamics between 1960 and 2010: Continental trends and intra-basin sensitivity. *Glob.*
978 *Planet. Change* 115, 44–58. <https://doi.org/10.1016/j.gloplacha.2014.01.011>
- 979 Cohen, S., Kettner, A.J., Syvitski, J.P.M., Fekete, B.M., 2013. WBMsed, a distributed global-
980 scale riverine sediment flux model: Model description and validation. *Comput. Geosci.* 53,
981 80–93. <https://doi.org/10.1016/j.cageo.2011.08.011>
- 982 Collischonn, W., Allasia, D., Da Silva, B.C., Tucci, C.E.M., 2007. The MGB-IPH model for
983 large-scale rainfall—runoff modelling. *Hydrol. Sci. J.* 52, 878–895.
984 <https://doi.org/10.1623/hysj.52.5.878>
- 985 Dearing, J.A., Jones, R.T., 2003. Coupling temporal and spatial dimensions of global sediment
986 flux through lake and marine sediment records. *Glob. Planet. Change* 39, 147–168.
987 [https://doi.org/10.1016/S0921-8181\(03\)00022-5](https://doi.org/10.1016/S0921-8181(03)00022-5)
- 988 Doetterl, S., Van Oost, K., Six, J., 2012. Towards constraining the magnitude of global
989 agricultural sediment and soil organic carbon fluxes. *Earth Surf. Process. Landforms* 37,
990 642–655. <https://doi.org/10.1002/esp.3198>
- 991 Fagundes, H. de O., Fan, F.M., Paiva, R.C.D., 2019. Automatic calibration of a large-scale
992 sediment model using suspended sediment concentration, water quality, and remote sensing
993 data. *Brazilian J. Water Resour.* 24, 1–18. [https://doi.org/10.1590/2318-](https://doi.org/10.1590/2318-0331.241920180127)
994 [0331.241920180127](https://doi.org/10.1590/2318-0331.241920180127)
- 995 Fagundes, H.O., Paiva, R.C.D., Fan, F.M., Buarque, D.C., Fassoni-Andrade, A.C., 2020.
996 Sediment modeling of a large-scale basin supported by remote sensing and in-situ
997 observations. *Catena* 190, 104535. <https://doi.org/10.1016/j.catena.2020.104535>
- 998 Fan, F.M., Buarque, D.C., Pontes, P.R.M., Collischonn, W., 2015. Um Mapa de Unidades de
999 Resposta Hidrológica para a América do Sul. XXI Simpósio Bras. e Recur. Hídricos 1–8.
- 1000 FAO/UNESCO, 1974. FAO/UNESCO Soil Map of the World | Food and Agriculture
1001 Organization of the United Nations [WWW Document]. FAO/UNESCO Soil Map World.
- 1002 Fassoni-Andrade, A.C., Paiva, R.C.D. de, 2019a. Mapping spatial-temporal sediment dynamics
1003 of river-floodplains in the Amazon. *Remote Sens. Environ.* 221, 94–107.
1004 <https://doi.org/10.1016/j.rse.2018.10.038>
- 1005 Fassoni-Andrade, A.C., Paiva, R.C.D. de, 2019b. Mapping spatial-temporal sediment dynamics
1006 of river-floodplains in the Amazon. *Remote Sens. Environ.* 221, 94–107.
1007 <https://doi.org/10.1016/j.rse.2018.10.038>
- 1008 Filizola, N., Guyot, J.-L., Wittmann, H., Martinez, J.-M., de, E., 2011. The Significance of
1009 Suspended Sediment Transport Determination on the Amazonian Hydrological Scenario.
1010 *Sediment Transp. Aquat. Environ.* <https://doi.org/10.5772/19948>
- 1011 Filizola, N., Guyot, J.L., 2011. Fluxo de sedimentos em suspensão nos rios da Amazônia. *Rev.*
1012 *Bras. Geociências* 41, 566–576.
- 1013 Fleischmann, A., Collischonn, W., Paiva, R., Tucci, C.E., 2019a. Modeling the role of reservoirs
1014 versus floodplains on large-scale river hydrodynamics. *Nat. Hazards* 99, 1075–1104.
1015 <https://doi.org/10.1007/s11069-019-03797-9>
- 1016 Fleischmann, A., Paiva, R., Collischonn, W., 2019b. Can regional to continental river
1017 hydrodynamic models be locally relevant? A cross-scale comparison. *J. Hydrol.* X 3,
1018 100027. <https://doi.org/10.1016/j.hydroa.2019.100027>
- 1019 Fleischmann, A., Siqueira, V., Paris, A., Collischonn, W., Paiva, R., Pontes, P., Crétaux, J.F.,
1020 Bergé-Nguyen, M., Biancamaria, S., Gosset, M., Calmant, S., Tanimoun, B., 2018.
1021 Modelling hydrologic and hydrodynamic processes in basins with large semi-arid wetlands.
1022 *J. Hydrol.* 561, 943–959. <https://doi.org/10.1016/j.jhydrol.2018.04.041>

- 1023 Fluet-Chouinard, E., Lehner, B., Rebelo, L.M., Papa, F., Hamilton, S.K., 2015. Development of
1024 a global inundation map at high spatial resolution from topographic downscaling of coarse-
1025 scale remote sensing data. *Remote Sens. Environ.* 158, 348–361.
1026 <https://doi.org/dx.doi.org/10.1016/j.rse.2014.10.015>
- 1027 Föeüger, L.B., 2019. Modelagem Hidrossedimentológica de Grandes Bacias com Propagação
1028 Inercial de Vazão: estudo de caso da baica do rio Madeira. Federal University of Espirito
1029 Santo.
- 1030 Forsberg, B.R., Melack, J.M., Dunne, T., Barthem, R.B., Goulding, M., Paiva, R.C.D., Sorribas,
1031 M. V., Silva, U.L., Weisser, S., 2017. The potential impact of new Andean dams on
1032 Amazon fluvial ecosystems, *PLoS ONE*. <https://doi.org/10.1371/journal.pone.0182254>
- 1033 Galy, V., Peucker-Ehrenbrink, B., Eglinton, T., 2015. Global carbon export from the terrestrial
1034 biosphere controlled by erosion. *Nature* 521, 204–207. <https://doi.org/10.1038/nature14400>
- 1035 García-Ruiz, J.M., Beguería, S., Nadal-Romero, E., González-Hidalgo, J.C., Lana-Renault, N.,
1036 Sanjuán, Y., 2015. A meta-analysis of soil erosion rates across the world. *Geomorphology*
1037 239, 160–173. <https://doi.org/10.1016/j.geomorph.2015.03.008>
- 1038 Getirana, A.C. V, Paiva, R.C.D., 2013. Mapping large-scale river flow hydraulics in the Amazon
1039 Basin. *Water Resour. Res.* 49, 2437–2445. <https://doi.org/10.1002/wrcr.20212>
- 1040 Grill, G., Lehner, B., Thieme, M., Geenen, B., Tickner, D., Antonelli, F., Babu, S., Borrelli, P.,
1041 Cheng, L., Crochetiere, H., Ehalt Macedo, H., Filgueiras, R., Goichot, M., Higgins, J.,
1042 Hogan, Z., Lip, B., McClain, M.E., Meng, J., Mulligan, M., Nilsson, C., Olden, J.D.,
1043 Opperman, J.J., Petry, P., Reidy Liermann, C., Sáenz, L., Salinas-Rodríguez, S., Schelle, P.,
1044 Schmitt, R.J.P., Snider, J., Tan, F., Tockner, K., Valdujo, P.H., van Soesbergen, A., Zarfl,
1045 C., 2019. Mapping the world’s free-flowing rivers. *Nature* 569, 215–221.
1046 <https://doi.org/10.1038/s41586-019-1111-9>
- 1047 Guyot, J., Bourges, J., Calle, H., Cortes, J., Hoorelbecke, R., Roche, M., 1989. Transport of
1048 suspended sediments to the Amazon by the Andean river: The River Mamore, Bolivia, in:
1049 Fourth International Symposium on River Sedimentation. ISRS, Beijing, China. pp. 106–
1050 113.
- 1051 Guyot, J.L., Filizola, N., Quintanilla, J., Cortez, J., 1996. Dissolved solids and suspended
1052 sediment yields in the Rio Madeira basin, from the Bolivian Andes to the Amazon. *IAHS-
1053 AISH Publ.* 236, 55–63.
- 1054 Guyot, J.L., Jouanneau, J.M., Wasson, J.G., 1999. Characterisation of river bed and suspended
1055 sediments in the Rio Madeira drainage basin (Bolivian Amazonia). *J. South Am. Earth Sci.*
1056 12, 401–410. [https://doi.org/10.1016/S0895-9811\(99\)00030-9](https://doi.org/10.1016/S0895-9811(99)00030-9)
- 1057 Hanasaki, N., Kanae, S., Oki, T., 2006. A reservoir operation scheme for global river routing
1058 models. *J. Hydrol.* 327, 22–41.
- 1059 Hanasaki, N., Kanae, S., Oki, T., Masuda, K., Motoya, K., Shirakawa, N., Shen, Y., Tanaka, K.,
1060 2008. An integrated model for the assessment of global water resources – Part 1: Model
1061 description and input meteorological forcing. *Hydrol. Earth Syst. Sci.* 12, 1007–1025.
- 1062 Hanasaki, N., Kanae, S., Oki, T., Masuda, K., Motoya, K., Shirakawa, N., Shen, Y., Tanaka, K.,
1063 2008. An integrated model for the assessment of global water resources – Part 2:
1064 Applications and assessments. *Hydrol. Earth Syst. Sci.* 12, 1027–1037.
- 1065 Hanasaki, N., Yoshikawa, S., Pokhrel, Y., Kanae, S., 2018. A global hydrological simulation to
1066 specify the sources of water used by humans. *Hydrol. Earth Syst. Sci.* 22, 789–817.
- 1067 Ito, A., 2007. Simulated impacts of climate and land-cover change on soil erosion and
1068 implication for the carbon cycle, 1901 to 2100. *Geophys. Res. Lett.*

- 1069 <https://doi.org/10.1029/2007GL029342>
- 1070 Kettner, A.J., Restrepo, J.D., Syvitski, J.P.M., 2010. A spatial simulation experiment to replicate
1071 fluvial sediment fluxes within the Magdalena River Basin, Colombia. *J. Geol.* 118, 363–
1072 379. <https://doi.org/10.1086/652659>
- 1073 Knisel, W.G., 1980. CREAMS: A Field-Scale Model for Chemicals, Runoff and Erosion for
1074 Agricultural Management Systems.
- 1075 Kollat, J.B., Reed, P.M., Wagener, T., 2012. When are multiobjective calibration trade-offs in
1076 hydrologic models meaningful? *Water Resour. Res.* 48, 1–19.
1077 <https://doi.org/10.1029/2011WR011534>
- 1078 Kouwen, N., Soulis, E.D., Pietroniro, A., Donald, J., HARRINGTON; R. A., 1993. Grouped
1079 Response Units for Distributed Hydrologic Modeling. *J. Water Resour. Plan. Manag.* 119,
1080 289–305.
- 1081 Krysanova, V., Mu, D., Becker, A., 1998. Development and test of a spatially distributed
1082 hydrological/ water quality model for mesoscale watersheds. *Ecol. Model* 106, 261–289.
- 1083 Kuhn, N.J., Hoffmann, T., Schwanghat, W., Dotterwiech, M., 2009. Agricultural soil erosion and
1084 global carbon cycle: controversy over? *Earth Surf. Process. Landforms* 34, 1033–1038.
1085 <https://doi.org/10.1002/esp>
- 1086 Lal, R., 2003. Soil erosion and the global carbon budget. *Environ. Int.* 29, 437–450.
1087 [https://doi.org/10.1016/S0160-4120\(02\)00192-7](https://doi.org/10.1016/S0160-4120(02)00192-7)
- 1088 Latrubesse, E.M., Arima, E.Y., Dunne, T., Park, E., Baker, V.R., D’Horta, F.M., Wight, C.,
1089 Wittmann, F., Zuanon, J., Baker, P.A., Ribas, C.C., Norgaard, R.B., Filizola, N., Ansar, A.,
1090 Flyvbjerg, B., Stevaux, J.C., 2017. Damming the rivers of the Amazon basin. *Nature* 546,
1091 363–369. <https://doi.org/10.1038/nature22333>
- 1092 Latrubesse, E.M., Stevaux, J.C., Sinha, R., 2005. Tropical rivers. *Geomorphology* 70, 187–206.
1093 <https://doi.org/10.1016/j.geomorph.2005.02.005>
- 1094 Lehner, B., Liermann, C.R., Revenga, C., Vörösmarty, C., Fekete, B., Crouzet, P., Döll, P.,
1095 Endejan, M., Frenken, K., Magome, J., Nilsson, C., Robertson, J.C., Rödel, R., Sindorf, N.,
1096 Wisser, D., 2011. High-resolution mapping of the world’s reservoirs and dams for
1097 sustainable river-flow management. *Front. Ecol. Environ.* 9, 494–502.
1098 <https://doi.org/10.1890/100125>
- 1099 Lehner, B., Verdin, K., Jarvis, A., 2008. New global hydrography derived from spaceborne
1100 elevation data. *Eos (Washington, DC)*. 89, 93–94.
1101 <https://doi.org/https://doi.org/10.1029/2008EO100001>
- 1102 Lima, J.E.F.W., Lopes, W.T. a., De Oliveira Carvalho, N., Vieira, M.R., Da Silva, E.M., 2005.
1103 Suspended sediment fluxes in the large river basins of Brazil. *IAHS ICCE Symp. Sediments*
1104 *Budgets* 1 1, 355–364.
- 1105 Littleboy, M., Silburn, M.D., Freebairn, D.M., Woodruff, D.R., Hammer, G.L., Leslie, J.K.,
1106 1992. Impact of soil erosion on production in cropping systems. I. Development and
1107 validation of a simulation model. *Aust. J. Soil Res.* 30, 757–774.
- 1108 Martín-Vide, J.P., Amarilla, M., Zárata, F.J., 2014. Collapse of the Pilcomayo River.
1109 *Geomorphology* 205, 155–163. <https://doi.org/10.1016/j.geomorph.2012.12.007>
- 1110 Morehead, M.D., Syvitski, J.P., Hutton, E.W.H., Peckham, S.D., 2003. Modeling the temporal
1111 variability in the flux of sediment from ungauged river basins. *Glob. Planet. Change* 39, 95–
1112 110. [https://doi.org/10.1016/S0921-8181\(03\)00019-5](https://doi.org/10.1016/S0921-8181(03)00019-5)
- 1113 Morris, G., Fan, J., 1998. *Reservoir Sedimentation Handbook*. McGraw-Hill Book Co., New
1114 York.

- 1115 Mouyen, M., Longuevergne, L., Steer, P., Crave, A., Lemoine, J.M., Save, H., Robin, C., 2018.
1116 Assessing modern river sediment discharge to the ocean using satellite gravimetry. *Nat.*
1117 *Commun.* 9, 1–9. <https://doi.org/10.1038/s41467-018-05921-y>
- 1118 Müller-Nedebock, D., Chaplot, V., 2015. Soil carbon losses by sheet erosion: A potentially
1119 critical contribution to the global carbon cycle. *Earth Surf. Process. Landforms* 40, 1803–
1120 1813. <https://doi.org/10.1002/esp.3758>
- 1121 Murphy, J., 2019. Declining suspended sediment in United States rivers and streams: Linking
1122 sediment trends to changes in land use/cover, hydrology and climate. *Hydrol. Earth Syst.*
1123 *Sci. Discuss.* 1–37. <https://doi.org/10.5194/hess-2019-435>
- 1124 Naipal, V., Ciais, P., Wang, Y., Lauerwald, R., Guenet, B., Van Oost, K., 2018. Global soil
1125 organic carbon removal by water erosion under climate change and land use change during
1126 AD-1850-2005. *Biogeosciences* 15, 4459–4480. <https://doi.org/10.5194/bg-15-4459-2018>
- 1127 Naipal, V., Reick, C., Pongratz, J., Van Oost, K., 2015. Improving the global applicability of the
1128 RUSLE model - Adjustment of the topographical and rainfall erosivity factors. *Geosci.*
1129 *Model Dev.* 8, 2893–2913. <https://doi.org/10.5194/gmd-8-2893-2015>
- 1130 Nash, J.E., Sutcliffe, J. V., 1970. River Flow Forecasting Through Conceptual Models Part I-a
1131 Discussion of Principles. *J. Hydrol.* 10, 282–290. [https://doi.org/10.1016/0022-](https://doi.org/10.1016/0022-1694(70)90255-6)
1132 [1694\(70\)90255-6](https://doi.org/10.1016/0022-1694(70)90255-6)
- 1133 New, M., Lister, D., Hulme, M., Makin, I., 2002. A high-resolution data set of surface climate
1134 over global land areas. *Clim. Res.* 21, 1–25.
- 1135 Niu, B., Hong, S., Yuan, J., Peng, S., Wang, Z., Zhang, X., 2014. Global trends in sediment-
1136 related research in earth science during 1992-2011: A bibliometric analysis. *Scientometrics*
1137 98, 511–529. <https://doi.org/10.1007/s11192-013-1065-x>
- 1138 O’Loughlin, F.E., Paiva, R.C.D., Durand, M., Alsdorf, D.E., Bates, P.D., 2016. A multi-sensor
1139 approach towards a global vegetation corrected SRTM DEM product. *Remote Sens.*
1140 *Environ.* 182, 49–59.
- 1141 Oliveira, P.T.S., Nearing, M.A., Wendland, E., 2015. Orders of magnitude increase in soil
1142 erosion associated with land use change from native to cultivated vegetation in a Brazilian
1143 savannah environment. *Earth Surf. Process. Landforms* 40, 1524–1532.
1144 <https://doi.org/10.1002/esp.3738>
- 1145 Paiva, R.C.D., Buarque, D.C., Collischonn, W., Bonnet, M.P., Frappart, F., Calmant, S.,
1146 Bulh?es Mendes, C.A., 2013. Large-scale hydrologic and hydrodynamic modeling of the
1147 Amazon River basin. *Water Resour. Res.* 49, 1226–1243.
1148 <https://doi.org/10.1002/wrcr.20067>
- 1149 Paiva, R.C.D., Collischonn, W., Tucci, C.E.M., 2011. Large scale hydrologic and hydrodynamic
1150 modeling using limited data and a GIS based approach. *J. Hydrol.* 406, 170–181.
1151 <https://doi.org/10.1016/j.jhydrol.2011.06.007>
- 1152 Panagos, P., Borrelli, P., Meusburger, K., Yu, B., Klik, A., Lim, K.J., Yang, J.E., Ni, J., Miao,
1153 C., Chattopadhyay, N., Sadeghi, S.H., Hazbavi, Z., Zabihi, M., Larionov, G.A., Krasnov,
1154 S.F., Gorobets, A. V., Levi, Y., Erpul, G., Birkel, C., Hoyos, N., Naipal, V., Oliveira,
1155 P.T.S., Bonilla, C.A., Meddi, M., Nel, W., Al Dashti, H., Boni, M., Diodato, N., Van Oost,
1156 K., Nearing, M., Ballabio, C., 2017. Global rainfall erosivity assessment based on high-
1157 temporal resolution rainfall records. *Sci. Rep.* 7, 1–12. [https://doi.org/10.1038/s41598-017-](https://doi.org/10.1038/s41598-017-04282-8)
1158 [04282-8](https://doi.org/10.1038/s41598-017-04282-8)
- 1159 Panagos, P., Borrelli, P., Poesen, J., Ballabio, C., Lugato, E., Meusburger, K., Montanarella, L.,
1160 Alewell, C., 2015. The new assessment of soil loss by water erosion in Europe. *Environ.*

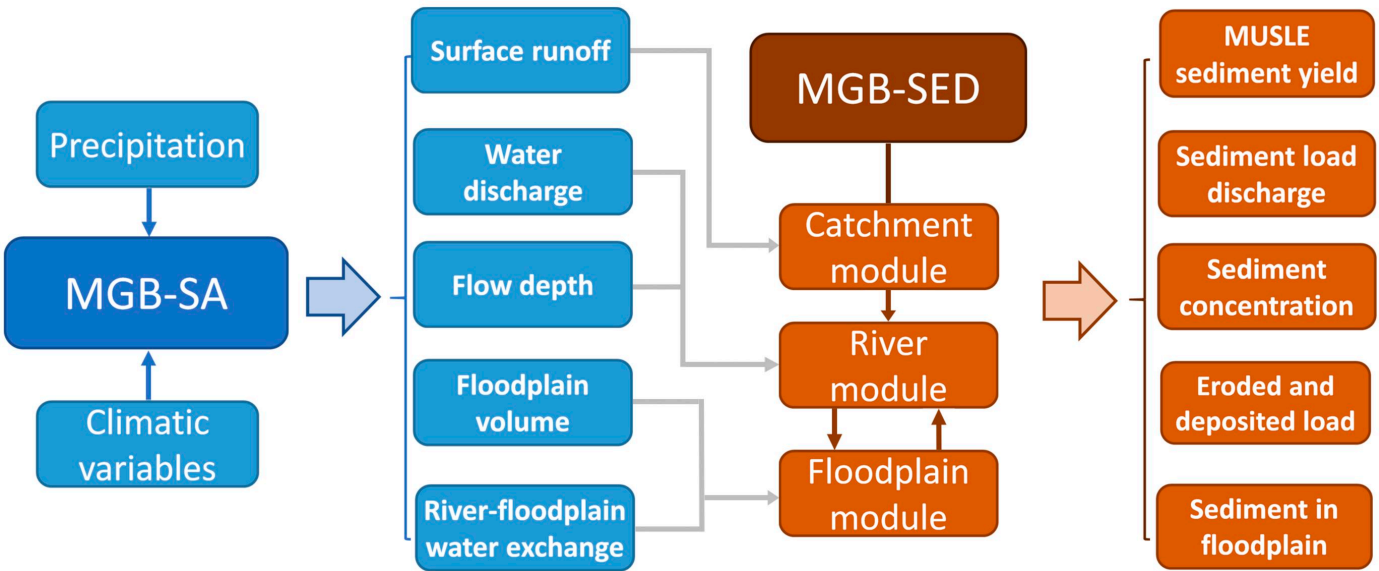
- 1161 Sci. Policy 54, 438–447. <https://doi.org/10.1016/j.envsci.2015.08.012>
- 1162 Pelletier, J.D., 2012. A spatially distributed model for the long-term suspended sediment
1163 discharge and delivery ratio of drainage basins. *J. Geophys. Res. Earth Surf.* 117, 1–15.
1164 <https://doi.org/10.1029/2011JF002129>
- 1165 Phinzi, K., Ngetar, N.S., 2019. The assessment of water-borne erosion at catchment level using
1166 GIS-based RUSLE and remote sensing: A review. *Int. Soil Water Conserv. Res.*
1167 <https://doi.org/10.1016/j.iswcr.2018.12.002>
- 1168 Pontes, P.R.M., 2016. Modelagem hidrológica e hidrodinâmica integrada da bacia do Prata.
1169 Universidade Federal do Rio Grande do Sul.
- 1170 Pontes, P.R.M., Fan, F.M., Fleischmann, A.S., Paiva, R.C.D., Buarque, D.C., Siqueira, V.A.,
1171 Jardim, P.F., Sorribas, M.V., Collischonn, W., 2017. MGB-IPH model for hydrological and
1172 hydraulic simulation of large floodplain river systems coupled with open source GIS.
1173 *Environ. Model. Softw.* 94, 1–20.
- 1174 Restrepo, J.D., Kjerfve, B., Hermelin, M., Restrepo, J.C., 2006. Factors controlling sediment
1175 yield in a major South American drainage basin: The Magdalena River, Colombia. *J.*
1176 *Hydrol.* 316, 213–232. <https://doi.org/10.1016/j.jhydrol.2005.05.002>
- 1177 Rivera, I.A., Cardenas, E.A., Espinoza-Villar, R., Espinoza, J.C., Molina-Carpio, J., Ayala, J.M.,
1178 Gutierrez-Cori, O., Martinez, J.M., Filizola, N., 2019. Decline of fine suspended sediments
1179 in the Madeira River basin (2003-2017). *Water (Switzerland)* 11.
1180 <https://doi.org/10.3390/w11030514>
- 1181 Rudorff, C.M., Dunne, T., Melack, J.M., 2018. Recent increase of river–floodplain suspended
1182 sediment exchange in a reach of the lower Amazon River. *Earth Surf. Process. Landforms*
1183 43, 322–332. <https://doi.org/10.1002/esp.4247>
- 1184 Sadeghi, S.H.R., Gholami, L., Khaledi Darvishan, A., Saeidi, P., 2014. A review of the
1185 application of the MUSLE model worldwide. *Hydrol. Sci. J.* 59, 365–375.
1186 <https://doi.org/10.1080/02626667.2013.866239>
- 1187 Sartori, M., Philippidis, G., Ferrari, E., Borrelli, P., Lugato, E., Montanarella, L., Panagos, P.,
1188 2019. A linkage between the biophysical and the economic: Assessing the global market
1189 impacts of soil erosion. *Land use policy* 86, 299–312.
1190 <https://doi.org/10.1016/j.landusepol.2019.05.014>
- 1191 Shen, Z.Y., Chen, L., Chen, T., 2012. Analysis of parameter uncertainty in hydrological
1192 modeling using GLUE method: a case study of SWAT model applied to Three Gorges
1193 Reservoir Region, China. *Hydrol. Earth Syst. Sci. Discuss.* 8, 8203–8229.
1194 <https://doi.org/10.5194/hessd-8-8203-2011>
- 1195 Shin, S., Pokhrel, Y., Miguez-Macho, G., 2019. High-resolution modeling of reservoir release
1196 and storage dynamics at the continental scale. *Water Resources Res.* 55, 787–810.
- 1197 Siqueira, V.A., Paiva, R.C.D., Fleischmann, A.S., Fan, F.M., Anderson, L., Pontes, P.R.M.,
1198 Paris, A., Calmant, S., Collischonn, W., 2018. Toward continental hydrologic –
1199 hydrodynamic modeling in South America. *Hydrol. Earth Syst. Sci.* 22, 4815–4842.
1200 <https://doi.org/doi.org/10.5194/hess-22-4815-2018>
- 1201 Syvitski, J.P.M., Cohen, S., Kettner, A.J., Brakenridge, G.R., 2014. How important and different
1202 are tropical rivers? - An overview. *Geomorphology* 227, 5–17.
1203 <https://doi.org/10.1016/j.geomorph.2014.02.029>
- 1204 Syvitski, J.P.M., Milliman, J.D., 2007. Geology, Geography, and Humans Battle for Dominance
1205 over the Delivery of Fluvial Sediment to the Coastal Ocean. *J. Geol.* 115, 1–19.
1206 <https://doi.org/10.1086/509246>

- 1207 Syvitski, J.P.M., Vörösmarty, C.J., Kettner, A.J., Green, P., 2005. Impact of Humans on the Flux
1208 of Terrestrial Sediment to the Global Coastal Ocean. *Science* (80-). 308, 376–380.
- 1209 Tan, Z., Leung, L.R., Li, H., Tesfa, T., Vanmaercke, M., Poesen, J., Zhang, X., Lu, H.,
1210 Hartmann, J., 2017. A Global Data Analysis for Representing Sediment and Particulate
1211 Organic Carbon Yield in Earth System Models. *Water Resour. Res.* 53, 10674–10700.
1212 <https://doi.org/10.1002/2017WR020806>
- 1213 Tan, Z., Leung, L.R., Li, H.Y., Tesfa, T., 2018. Modeling Sediment Yield in Land Surface and
1214 Earth System Models: Model Comparison, Development, and Evaluation. *J. Adv. Model.*
1215 *Earth Syst.* 10, 2192–2213. <https://doi.org/10.1029/2017MS001270>
- 1216 van Beek, L.P.H., Wada, Y., Bierkens, M.F.P., 2011. Global monthly water stress: 1. Water
1217 balance and water availability. *Water Resources Res.* 47.
1218 <https://doi.org/doi:10.1029/2010WR009791>
- 1219 Van Oost, K., Quine, T.A., Govers, G., De Gryze, S., Six, J., Harden, J.W., Ritchie, J.C.,
1220 McCarty, G.W., Heckrath, G., Kosmas, C., Giraldez, J. V., Marques Da Silva, J.R., Merckx,
1221 R., 2007. The impact of agricultural soil erosion on the global carbon cycle. *Science* (80-).
1222 318, 626–629. <https://doi.org/10.1126/science.1145724>
- 1223 Villar, J.C.E., Ronchail, J., Guyot, J.L., Cochonneau, G., Filizola, N., Lavado, W., de Oliveira,
1224 E., Pombosa, R., Vauchel, P., 2008. Spatio-temporal rainfall variability in the Amazon
1225 basin countries (Brazil, Peru, Bolivia, Colombia, and Ecuador). *Int. J. Climatol.* 2009,
1226 1574–1594. <https://doi.org/10.1002/joc>
- 1227 Wada, Y., Wisser, D., Bierkens, M.F.P., 2014. Global modeling of withdrawal, allocation and
1228 consumptive use of surface water and groundwater resources. *Earth Syst. Dyn. Discuss.* 5,
1229 15–40.
- 1230 Wang, Z., Van Oost, K., 2019. Modeling global anthropogenic erosion in the Holocene.
1231 *Holocene* 29, 367–379. <https://doi.org/10.1177/0959683618816499>
- 1232 Willenbring, J.K., Von Blanckenburg, F., 2010. Long-term stability of global erosion rates and
1233 weathering during late-Cenozoic cooling. *Nature* 465, 211–214.
1234 <https://doi.org/10.1038/nature09044>
- 1235 Williams, J.R., 1995. The EPIC model, in: *Computer Models of Watershed Hydrology*. pp. 909–
1236 1000.
- 1237 Williams, J.R., 1975. SEDIMENT ROUTING FOR AGRICULTURAL WATERSHEDS '.
1238 *Water Resour. Bull.* 11.
- 1239 Wischmeier, W., Smith, D., 1978. Predicting rainfall erosion losses: a guide to conservation
1240 planning, U.S. Department of Agriculture Handbook No. 537.
1241 <https://doi.org/10.1029/TR039i002p00285>
- 1242 Wisser, D., Fekete, B.M., Vörösmarty, C.J., Schumann, A.H., 2010. Reconstructing 20th century
1243 global hydrography: A contribution to the Global Terrestrial Network- Hydrology (GTN-
1244 H). *Hydrol. Earth Syst. Sci.* 14, 1–24. <https://doi.org/10.5194/hess-14-1-2010>
- 1245 Wittmann, H., von Blanckenburg, F., Maurice, L., Guyot, J.-L., Filizola, N., Kubik, P.W., 2011.
1246 Sediment production and delivery in the Amazon River basin quantified by in situ produced
1247 cosmogenic nuclides and recent river loads. *Geol. Soc. Am. Bull.* 123, 934–950.
- 1248 Wood, E.F., Roundy, J.K., Troy, T.J., van Beek, L.P.H., Bierkens, M.F.P., Blyth, E., et al, 2011.
1249 Hyperresolution global land surface modeling: meeting a grand challenge for monitoring
1250 Earth's terrestrial water. *Water Resour. Res.* 47, 1–10.
- 1251 Wuepper, D., Borrelli, P., Finger, R., 2019. Countries and the global rate of soil erosion. *Nat.*
1252 *Sustain.* 1–5. <https://doi.org/10.1038/s41893-019-0438-4>

- 1253 Xiong, M., Sun, R., Chen, L., 2019. A global comparison of soil erosion associated with land use
1254 and climate type. *Geoderma* 343, 31–39. <https://doi.org/10.1016/j.geoderma.2019.02.013>
- 1255 Xiong, M., Sun, R., Chen, L., 2018. Effects of soil conservation techniques on water erosion
1256 control: A global analysis. *Sci. Total Environ.* 645, 753–760.
1257 <https://doi.org/10.1016/j.scitotenv.2018.07.124>
- 1258 Yamazaki, D., de Almeida, G.A.M., Bates, P.D., 2013. Improving computational efficiency in
1259 global river models by implementing the local inertial flow equation and a vector-based
1260 river network map. *Water Resources Res.* 49, 7221–7235.
- 1261 Yamazaki, D., Kanae, S., Kim, H., Oki, T., 2011. A physically based description of floodplain
1262 inundation dynamics in a global river routing model. *Water Resources Res.* 47.
- 1263 Yang, C.T., 1973. Incipient motion and sediment transport. *J. Hydraul. Eng* 10, 1679–1704.
- 1264 Yang, D., Kanae, S., Oki, T., Koike, T., Musiak, K., 2003. Global potential soil erosion with
1265 reference to land use and climate changes. *Hydrol. Process.* 17, 2913–2928.
1266 <https://doi.org/10.1002/hyp.1441>
- 1267 Yapo, P.O., Gupta, H.V., Sorooshian, S., 1998. Multi-objective global optimization for
1268 hydrologic models. *J. Hydrol.* 204, 83–97. [https://doi.org/10.1016/S0022-1694\(97\)00107-8](https://doi.org/10.1016/S0022-1694(97)00107-8)
- 1269 Zhang, K., Douglas, B.C., Leatherman, S.P., 2004. Global warming and coastal erosion. *Clim.*
1270 *Change* 64, 41–58. <https://doi.org/10.1023/B:CLIM.0000024690.32682.48>
- 1271 Zhao, F., Veldkamp, T.I.E., Frieler, K., Schewe, J., Ostberg, S., Willner, S., Schaubberger, B.,
1272 Gosling, S.N., Schmied, H.M., Portmann, F.T., Leng, G., Huang, M., Liu, X., Tang, Q.,
1273 Hanasaki, N., Biemans, H., Gerten, D., Satoh, Y., Pokhrel, Y., Stacke, T., Ciais, P., Chang,
1274 J., Ducharne, A., Guimberteau, M., Wada, Y., Kim, H., Yamazaki, D., 2017. The critical
1275 role of the routing scheme in simulating peak river discharge in global hydrological models.
1276 *Environ. Res. Lett.* 12. <https://doi.org/10.1088/1748-9326/aa7250>
1277

Figure 1.

Figure 2.



Hydrological processes

- Interception, evapotranspiration, infiltration
- Surface, subsurface and groundwater runoff

Hydrodynamic routing

- Rivers: Local Inertial Method linked to floodplain
- Floodplain storage (vertical hydrology processes)

Sediment processes

- Rill and interrill erosions
- Propagation from catchment to channel
- Routing by Exner and transport 1D equations
- Channel erosion and deposition
- Floodplain exchanges

Figure 3.

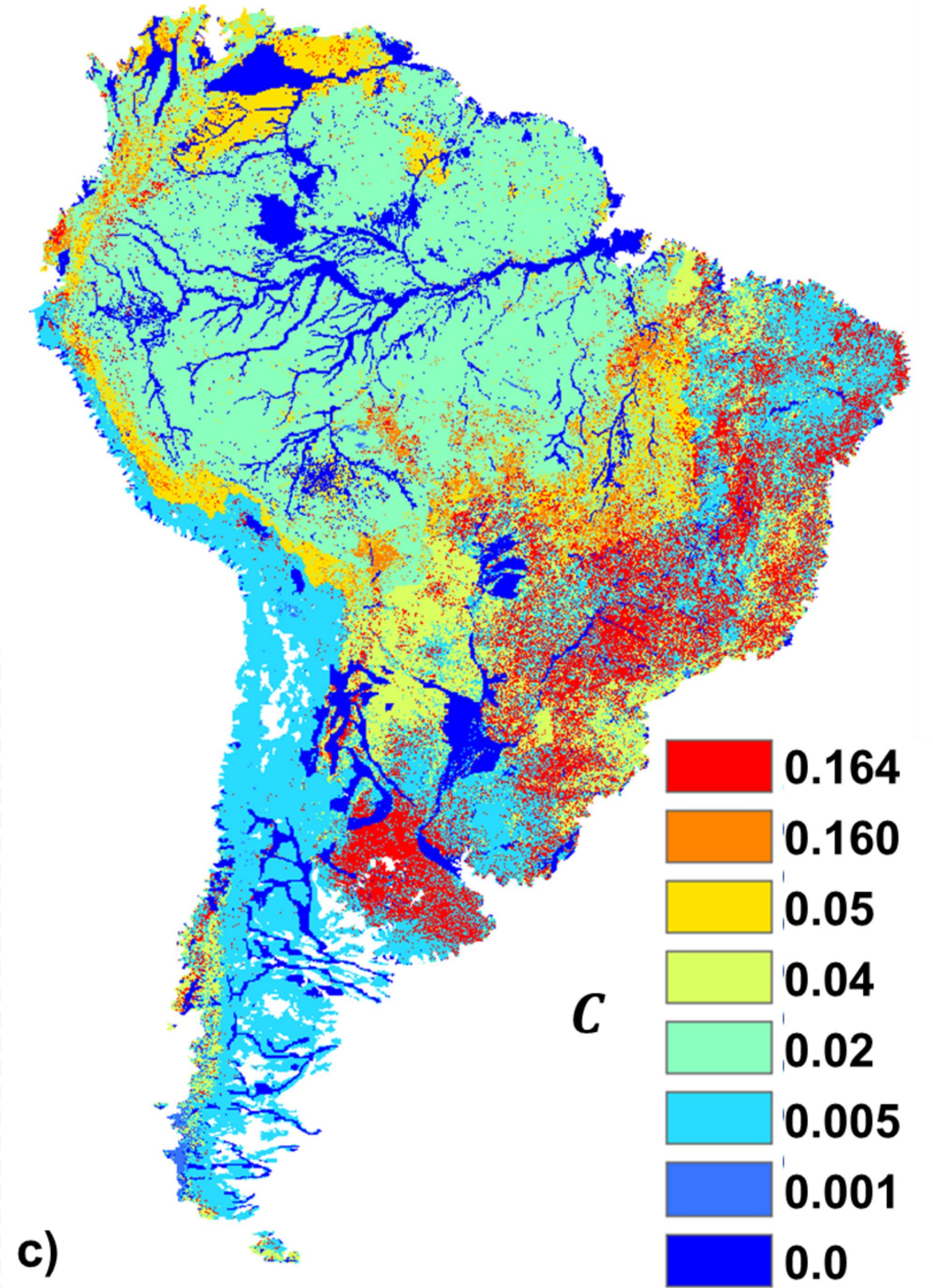
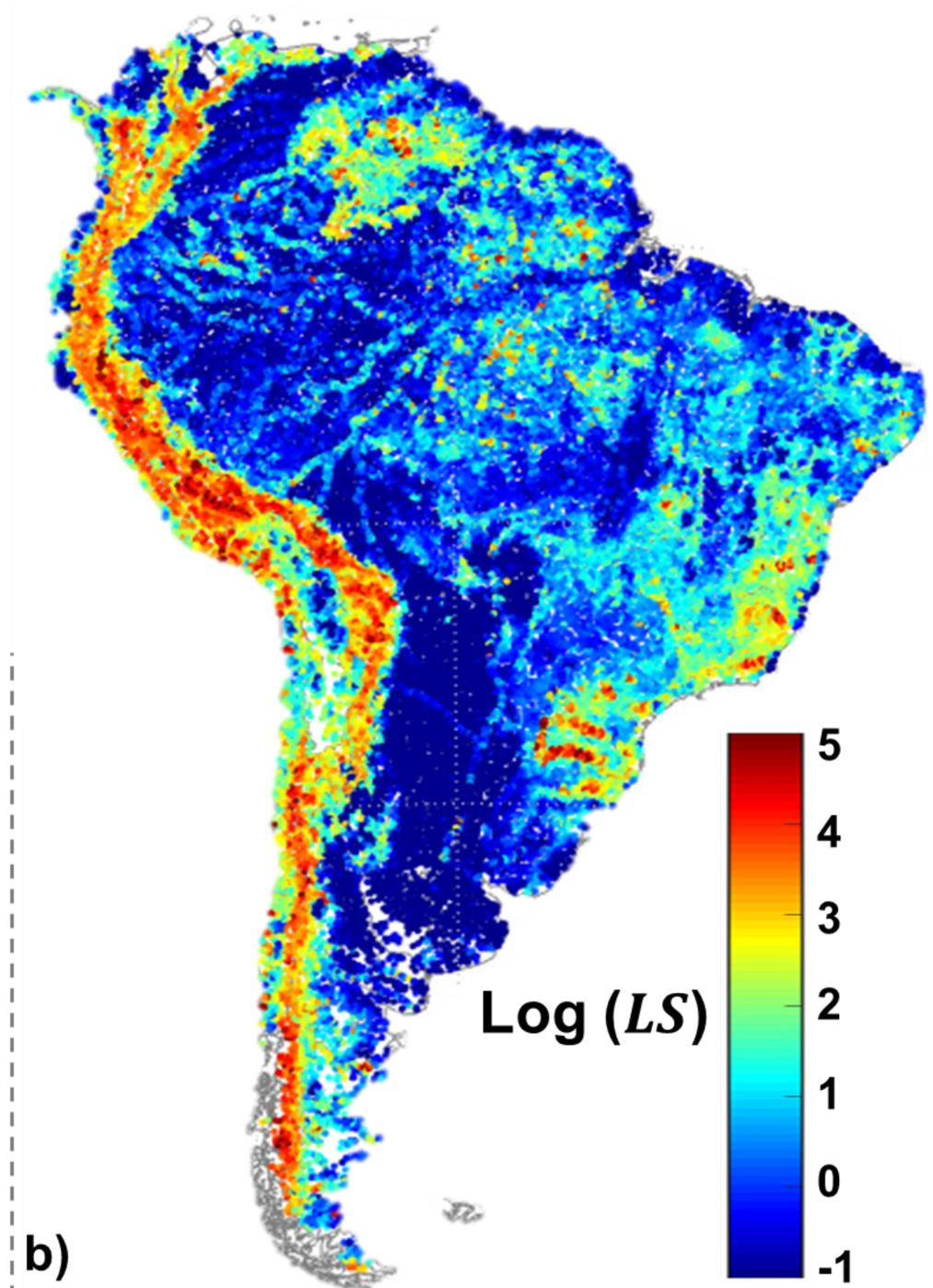
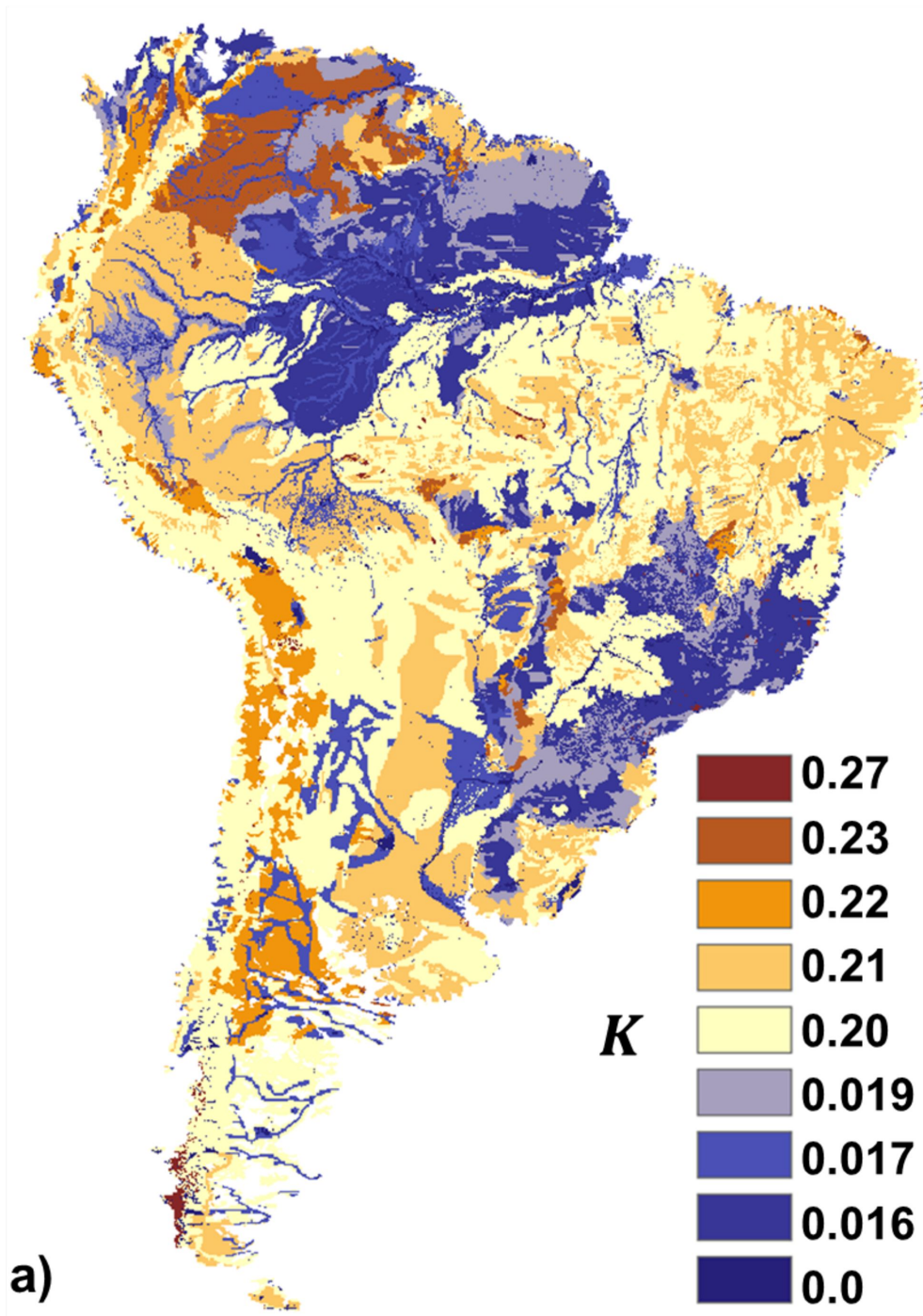
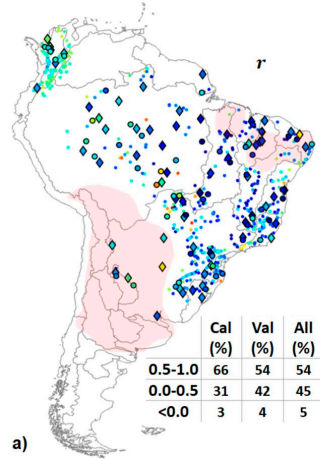
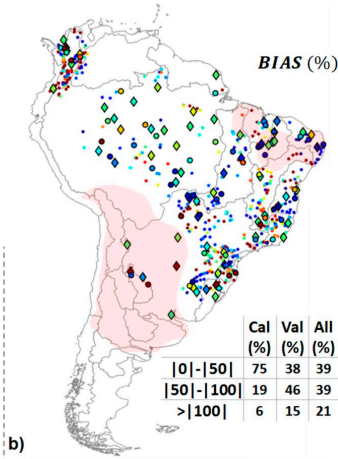


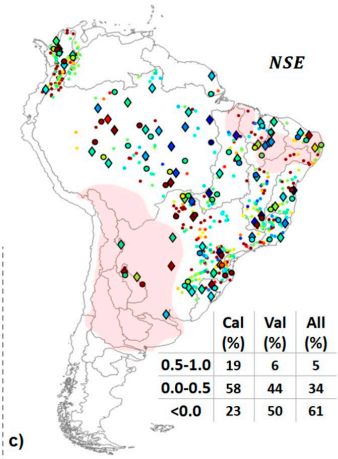
Figure 4.



-0.8 -0.4 0.0 0.4 0.8



-80 -40 0 40 80



-0.8 -0.4 0.0 0.4 0.8

Figure 5.

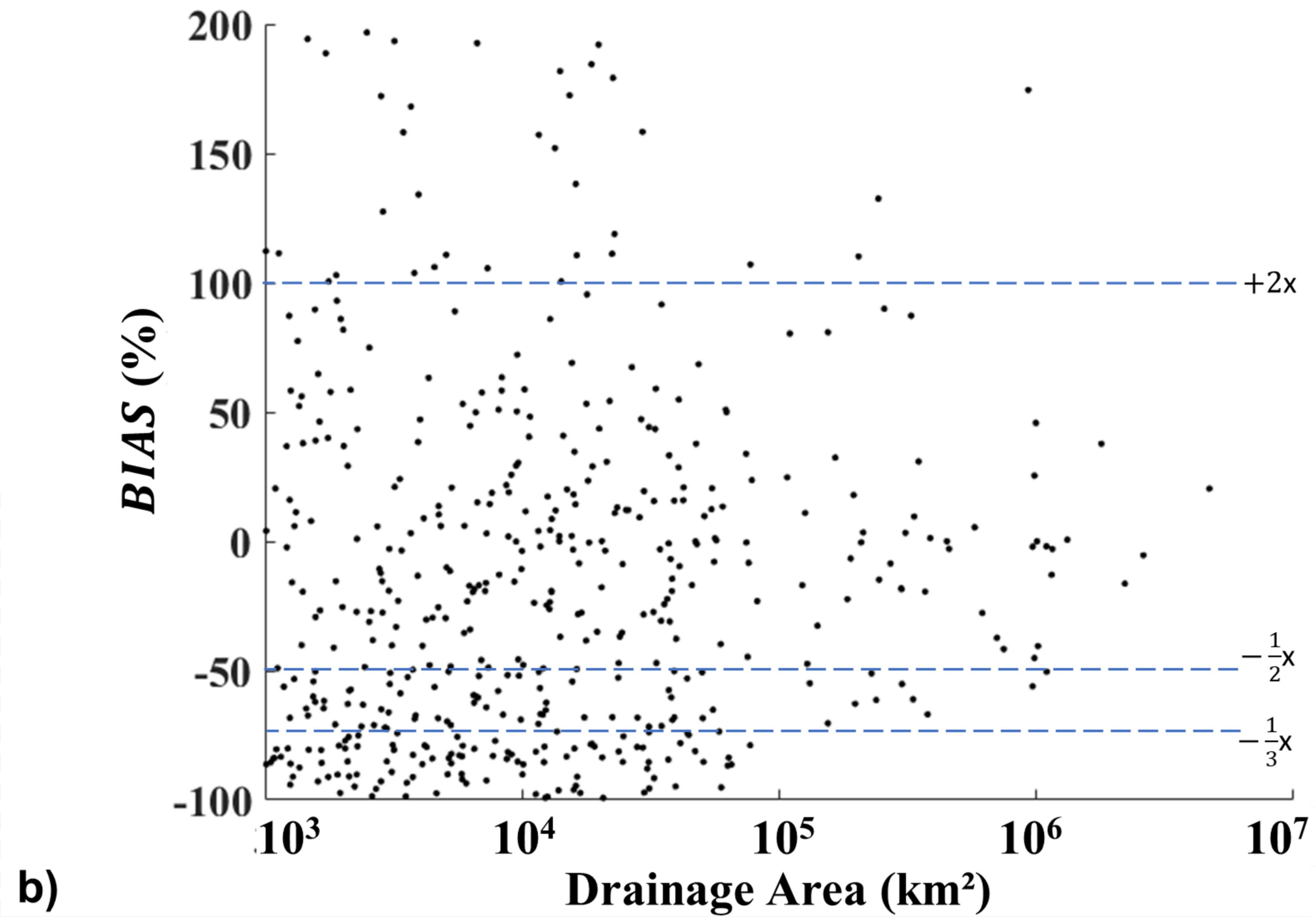
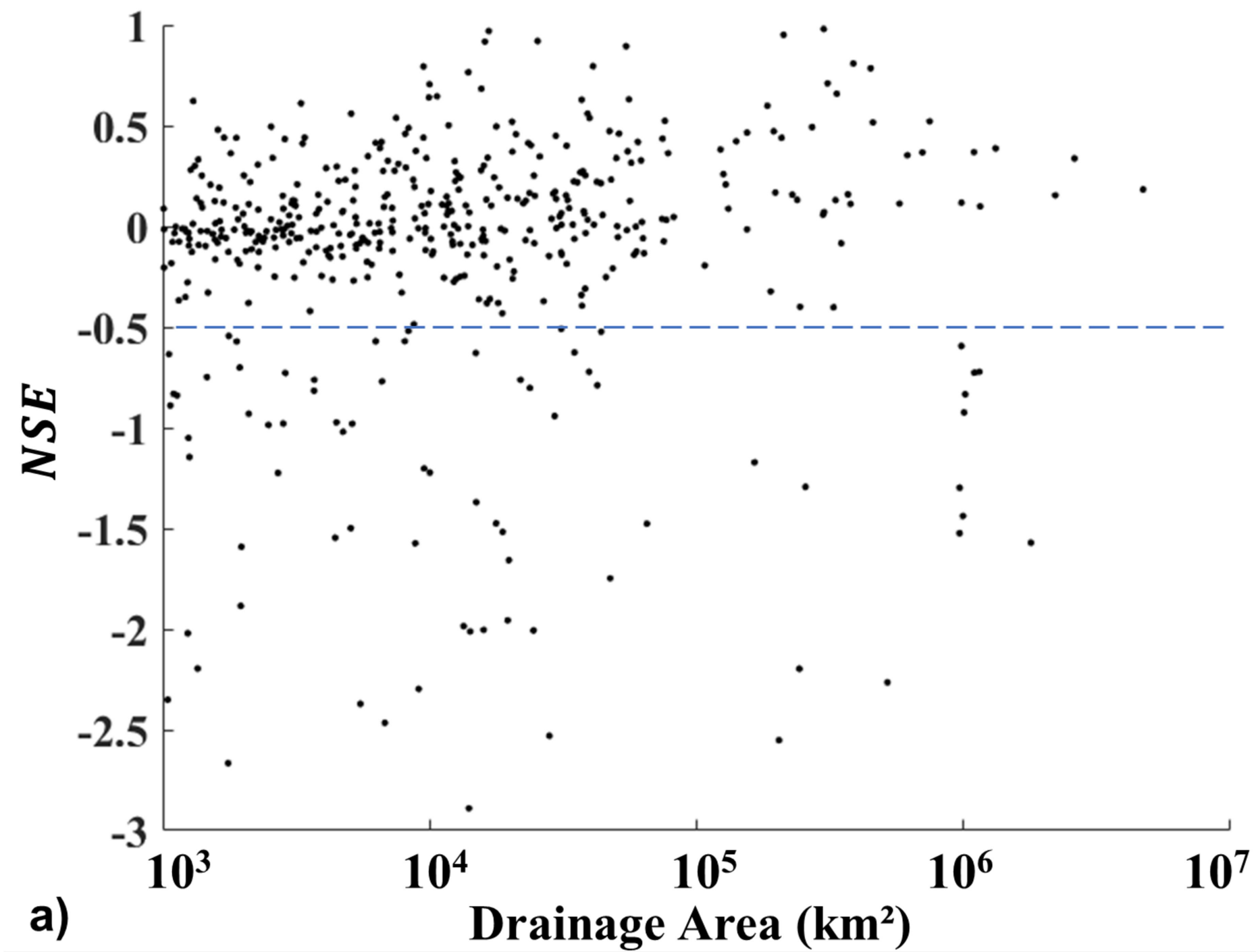


Figure 6.

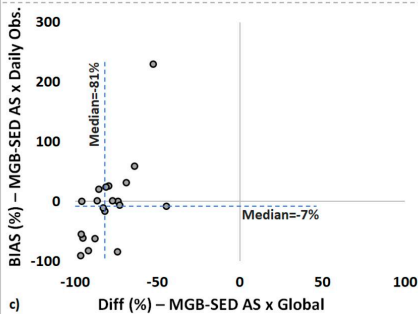
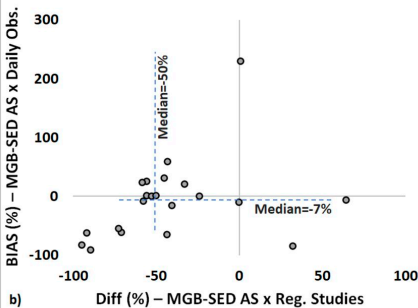
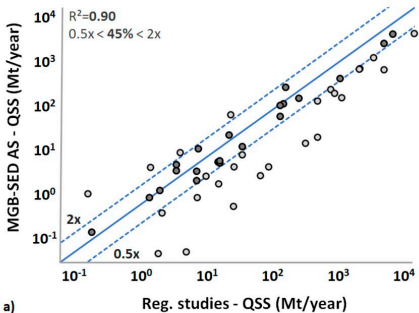
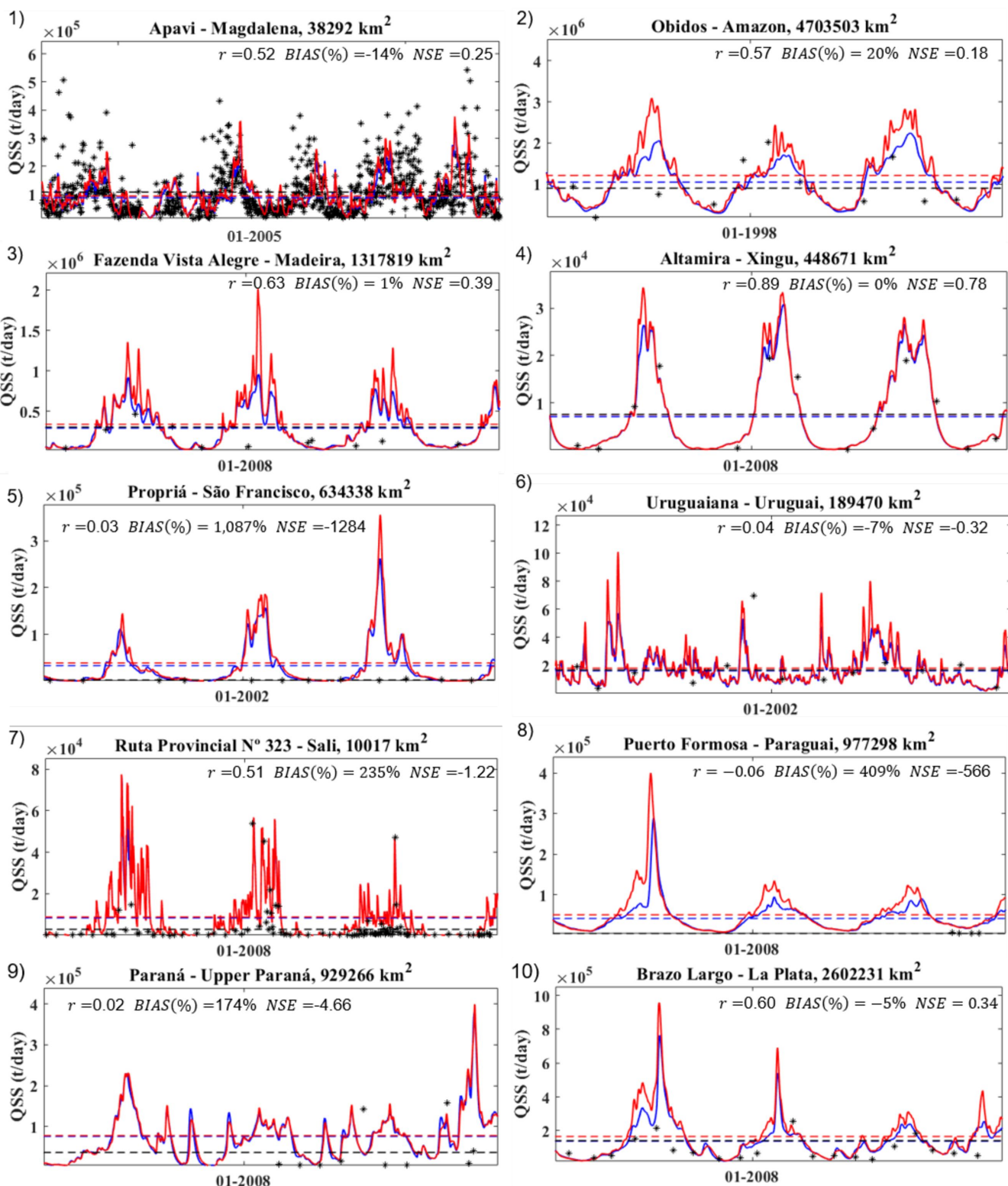


Figure 7.



— QSS IN

— QSS MC

* QSSObs

Figure 8.

Figure 9.

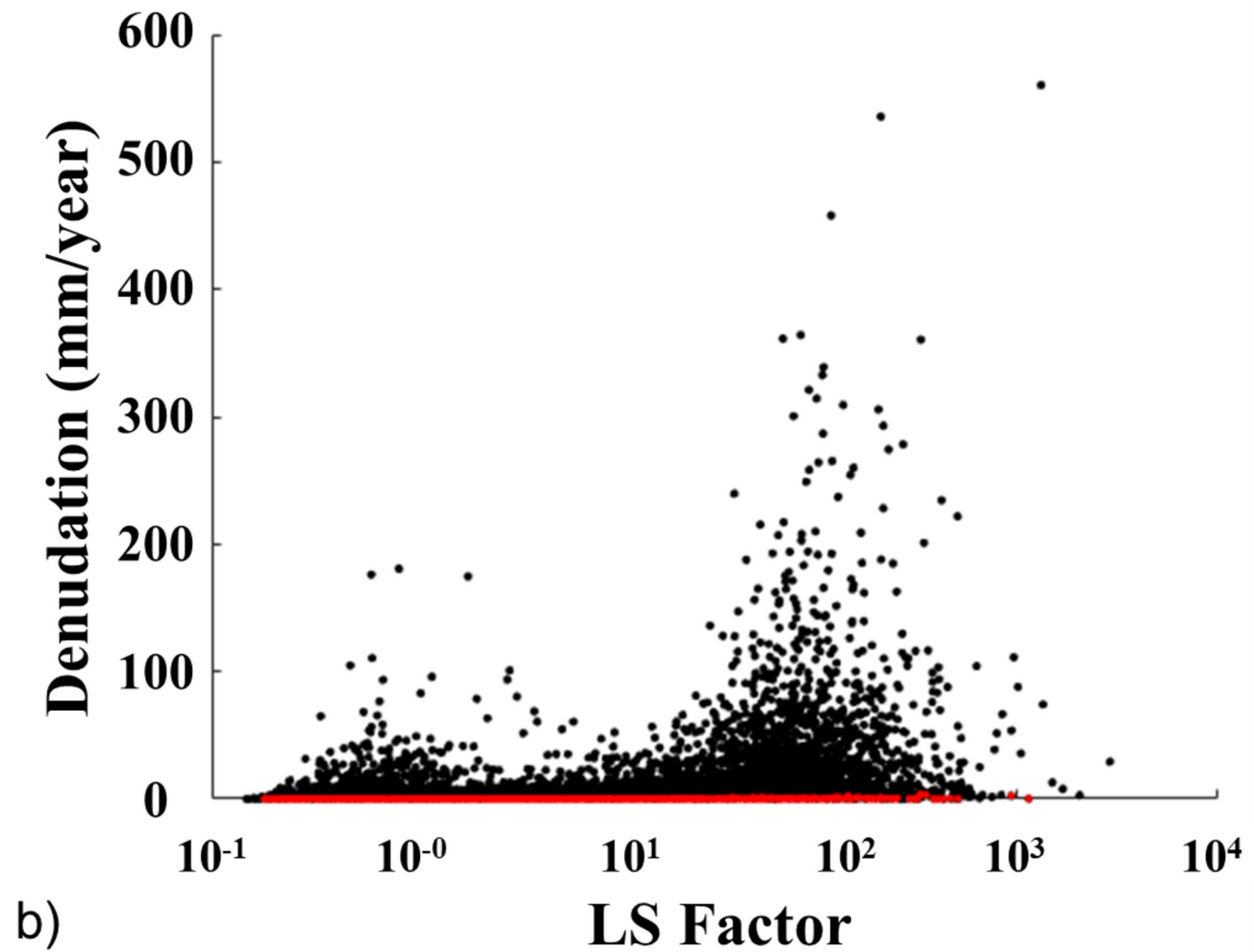
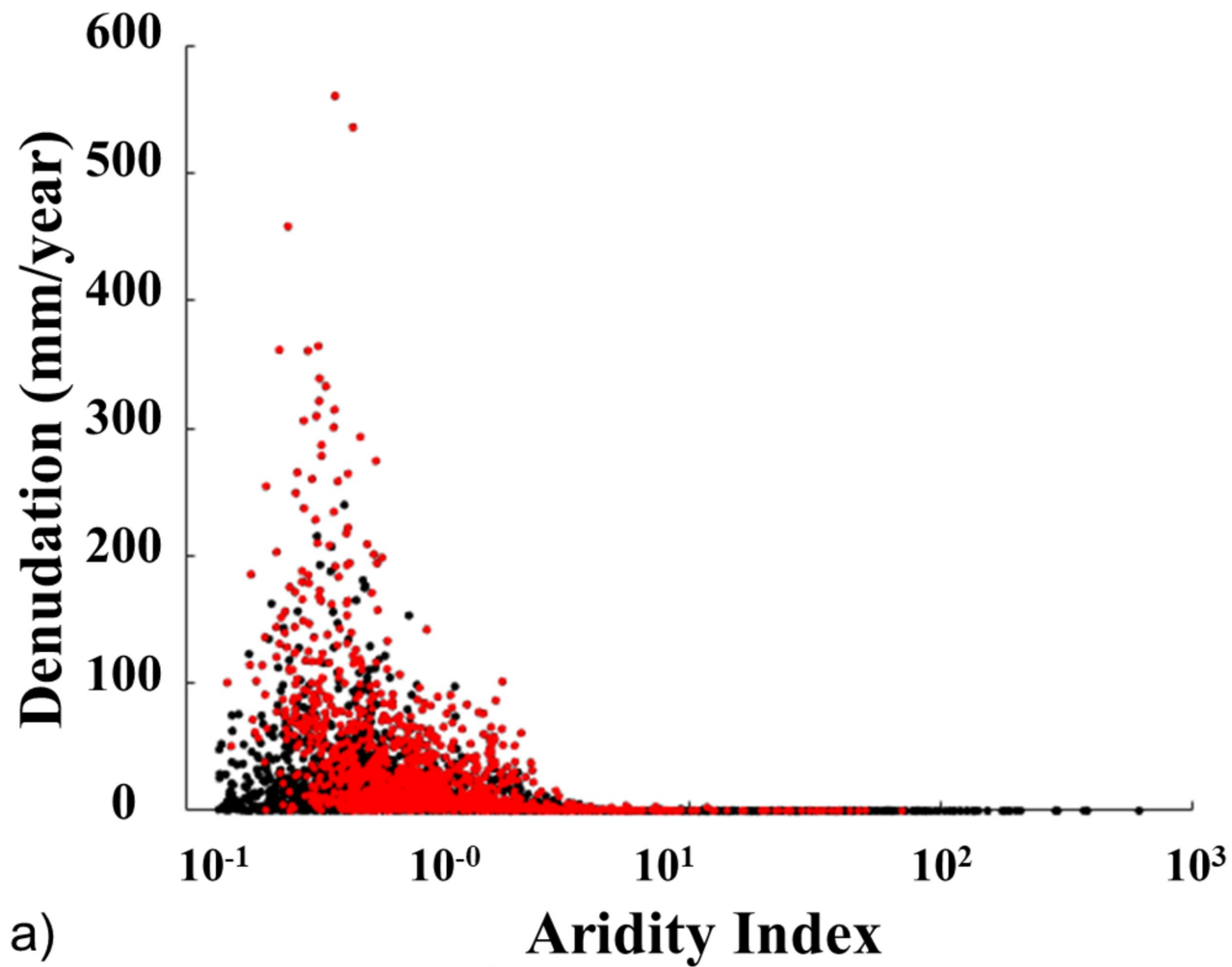


Figure 10.

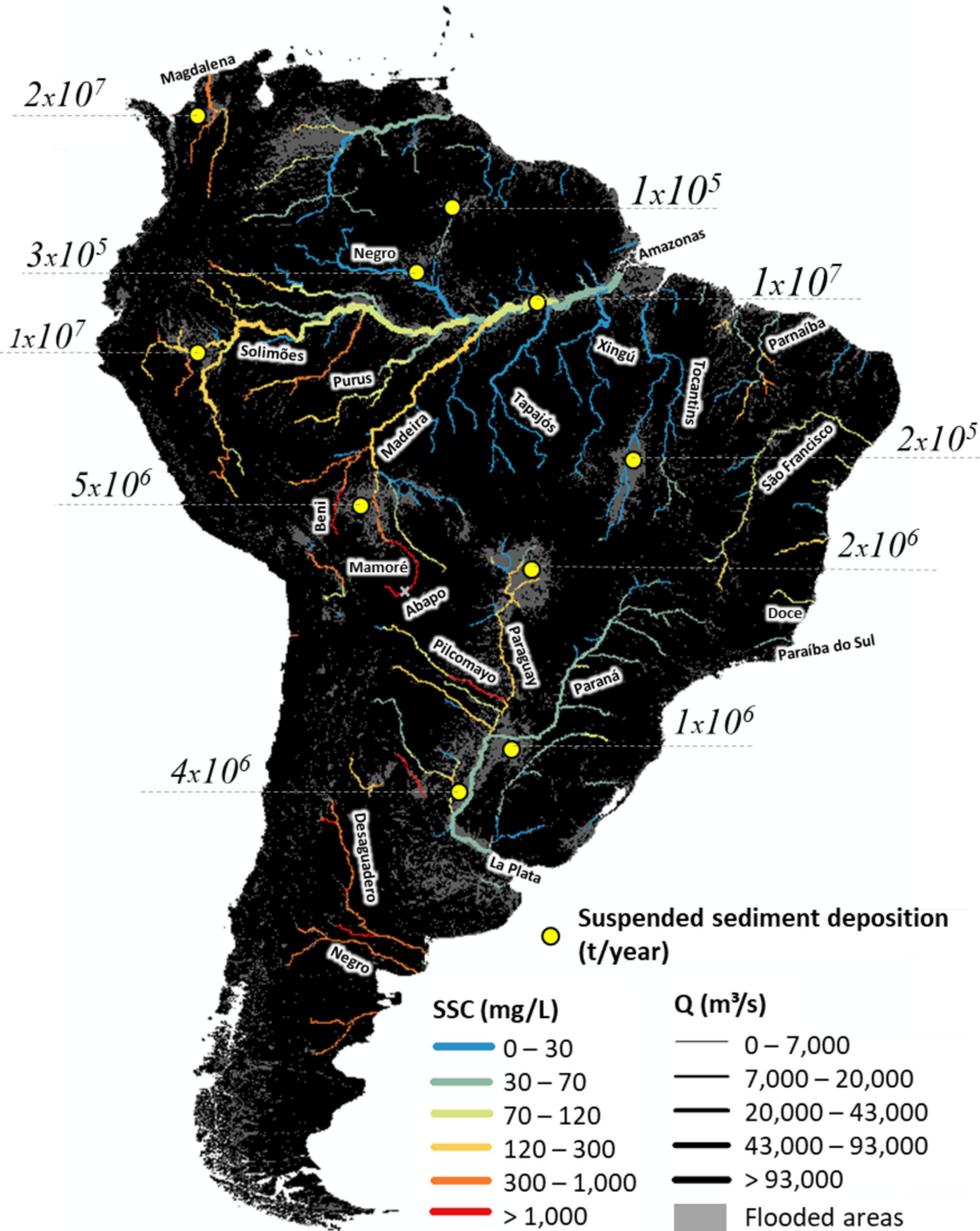


Figure 11.

